# Study of $\mu$s isomers in neutron-rich indium and cadmium isotopes

Inaugural-Dissertation
zur
Erlangung des Doktorgrades
der Mathematisch-Naturwissenschaftlichen Fakultät
der Universität zu Köln

vorgelegt von
**Antonella Scherillo**
aus Neapel, Italien

Köln 2005

| | |
|---|---|
| Berichterstatter: | Prof. Dr. Jan Jolie<br>Prof. Dr. Peter Reiter |
| Tag der mündlichen Prüfung: | 4 Februar 2005 |

# Abstract

Microsecond isomers in In and Cd isotopes, in the mass range $A = 123$ to 130, were investigated at the ILL reactor, Grenoble, through thermal-neutron induced fission reactions of Pu targets. The LOHENGRIN mass spectrometer has been used to select the recoiling fission fragments. The level schemes of the odd-even $^{123,125,127,129}$In and $^{125}$Cd, and new measurements of the $\mu$s half-lives of the odd-odd $^{126-130}$In are reported. However, the expected $8^+$ isomers in the even-even $^{126,128,130}$Cd isotopes were not observed. The comparisons between the experimental $B(M2)$ strengths for In and Sn isotopes are discussed. A shell-model study of the heaviest In and Cd nuclei was performed using a realistic interaction derived from the CD-Bonn nucleon-nucleon potential. The calculation predicts values of the half-lives of the first $8^+$ states in $^{126,128}$Cd of $\sim$ 10 ns, which could explain the non-observation of $\mu$s isomers. Comparison shows that the calculated levels of $^{130}$In and $^{129}$In are in good agreement with the experimental values, while some discrepancies occur for the lighter In isotopes. The collectivity of $^{126,128}$Cd is discussed in the framework of the shell model and in comparison with $^{204}$Hg. A theoretical prediction on $^{130}$Cd is reported.

# Kurzzusammenfassung

Am Forschungsreaktor des Institut Laue-Langevin, Grenoble, wurden Indium- und Cadmium-Isotope im Bereich der Massenzahlen $A = 123$ bis 130 untersucht mittels der durch thermische Neutronen induzierten Spaltung von Plutonium. Zur Trennung der Spaltfragmente wurde der LOHENGRIN-Massenseparator benutzt. Es wurden Termschemata für die ungerade-geraden Isotope $^{123,125,127,129}$In etabliert und im Mikrosekundenbereich neue Messungen der Lebensdauer angeregter Niveaus der ungerade-ungerade Kerne $^{126,128,130}$In durchgeführt. Die erwarteten $8^+$-Isomere in den gerade-gerade Isotopen $^{126,128,130}$Cd wurden nicht gefunden. Für Indium- und Zinn-Isotope wird der Vergleich der experimentellen $B(M2)$-Stärken diskutiert. Für die schwersten In- und Cd-Kerne wurden Schalenmodell-Rechnungen durchgeführt unter Verwendung einer realistischen Wechselwirkung, die aus dem CD-Bonn Kern-Kern-Potential abgeleitet ist. Diese Rechnungen sagen Halbwertszeiten des ersten $8^+$-Zustands in $^{126,128}$Cd von etwa 10 ns voraus, was erklärt, dass keine Isomere im Bereich von Mikrosekunden gefunden wurden. Ein Vergleich zeigt, dass die für $^{130}$In und $^{129}$In berechneten Niveaus in guter Übereinstimmung mit den experimentellen Werten sind, wogegen es für die leichteren Indium-Isotope einige Diskrepanzen gibt. Die Kollektivität von $^{126,128}$Cd wird im Rahmen des Schalenmodells und im Vergleich mit $^{204}$Hg diskutiert. Theoretische Vorhersagen über $^{130}$Cd werden angegeben.

*To my grandmother*

# Contents

**Contents** i

**List of Figures** 1

**List of Tables** 5

**Introduction** 7

**1 Motivation and theoretical background** 9
- 1.1 The region of $^{132}$Sn . . . 11
- 1.2 Nuclear Isomers . . . 12
  - 1.2.1 Spin isomers . . . 13
  - 1.2.2 Shape isomers . . . 14
  - 1.2.3 K isomers . . . 14
  - 1.2.4 Isomers due to low transition energy . . . 15
- 1.3 Weisskopf estimations for the lifetimes . . . 15
- 1.4 Conversion electrons . . . 16
- 1.5 The shell model . . . 17

**2 Experimental Technique** 21
- 2.1 Neutron-induced fission reactions as a tool to produce neutron-rich nuclei . . . 22
- 2.2 The LOHENGRIN mass separator . . . 27
- 2.3 Experimental set-up . . . 32
  - 2.3.1 The Clover detector . . . 35
  - 2.3.2 The Miniball detector . . . 35
- 2.4 Acquisition system and data analysis . . . 36
  - 2.4.1 Efficiency . . . 39

**3 Experimental Results** **41**
3.1 $^{123}$In . . . 41
3.2 $^{127}$In . . . 44
3.3 $^{129}$In . . . 46
3.4 Odd-odd Indium isotopes . . . 48
3.5 Cadmium isotopes . . . 50
3.5.1 $^{125}$Cd . . . 51
3.6 Level schemes of odd-In nuclei . . . 52
3.6.1 $^{129}$In . . . 54
3.6.2 $^{127}$In . . . 54
3.6.3 $^{125}$In . . . 55
3.6.4 $^{123}$In . . . 56

**4 Shell-model calculations and discussion** **57**
4.1 Shell model calculations . . . 57
4.2 Indium isotopes . . . 59
4.2.1 $^{129}$In . . . 59
4.2.2 $^{127}$In . . . 63
4.2.3 Odd-odd In nuclei . . . 64
4.2.4 $M2$ and $E3$ transition probabilities in Sn and In isotopes 65
4.3 Cadmium isotopes . . . 68
4.3.1 Even-even Cd isotopes . . . 68
4.3.2 $^{125}$Cd . . . 72

**Conclusions** **75**

**Bibliography** **79**

# List of Figures


1.1 Microseconds isomers in the vicinity of $^{132}$Sn. The half-lives indicated are in $\mu$s. . . . . 11

1.2 Potential energy versus deformation in the case of the existence of a second minimum . . . . . 14

1.3 Single particle level sequence for an Hamiltonian consisting of a central harmonic oscillator, a centrifugal $l^2$ term and a spin-orbit $l \cdot s$ term, taken from [22]. . . . . 19

2.1 A schematic diagram of the neutron-induced fission process with the approximate time-scale on which the phases occur. . 22

2.2 Mass yields of fission fragments for thermal-neutron induced fission of $^{235}$U, $^{238}$Np, $^{239}$Pu, $^{242}$Am, $^{245}$Cm and $^{249}$Cf. The data plotted, if existing, are measured at the LOHENGRIN mass separator. To complete the curve, the yields of some heavy masses are taken from the ENDF/B-VI database. Image provided by courtesy of Dr. Igor Tsekhanovich. . . . . 24

2.3 a) Picture of the LOHENGRIN mass separator. b) Schematic view of the LOHENGRIN mass separator. . . . . 28

2.4 $\Delta$E spectrum of the ions entering the ionization chamber. The LOHENGRIN separator was optimized for mass 123. . . . . 31

2.5 Schematic representation of the two experimental set-ups used to measure In and Cd isotopes. Experimental set-up 1: Ge1 and Ge2 are two 60 % HP germanium detectors, Si1 and Si2 are two adjacent cooled Si(Li) detector covering a total area of $2 \times 6$ cm$^2$. Experimental set-up 2: Ge1 is a Clover detector, Ge2 is a Miniball detector and $\Delta E1$, $\Delta E2$ are the fragment energies measured in the two stages of the ionization chamber. 33

2.6 $E_{tot} = \Delta E1 + \Delta E2$ versus $\Delta E_1$. LOHENGRIN was optimized for mass $A = 128$. . . . . 34
2.7 The Clover detector. . . . . 35
2.8 The Miniball detector. . . . . 36
2.9 Top part: Time distribution of mass $A = 123$. Bottom part: Germanium spectra obtained subtracting, after normalization, the spectrum in coincidence with region 2 from the spectrum in coincidence with region 1. Only the peaks belonging to $^{123}$In and $^{123}$Sn are labelled. . . . . 37
2.10 Top part: time distribution of mass $A = 123$. Bottom part: Germanium spectrum of the mass $A = 123$ corresponding to the whole time distribution. . . . . 38
2.11 Absolute efficiency of the Clover detector. . . . . 39

3.1 a) $\gamma$-decay spectrum of the mass $A$=123 in delayed coincidence with the fission fragments. b) Si(Li) spectrum of the mass $A$=123 in delayed coincidence with the fission fragments. The value 31.5 keV labelled is the energy of the isomeric transition. c) Time spectrum of 880.7, 1019.0, 1027.4 and 1166.0 keV. . . 42
3.2 $\gamma - \gamma$ coincidences between the four transitions of the isomeric cascade observed in $^{123}$In. . . . . 43
3.3 a) Coincidence spectra gated on the $\gamma$-ray of 233 or 221 keV. b) Si(Li) spectrum obtained in coincidence with the $\gamma$-rays of 221 and 233 keV. c) Time spectrum of 221 and 233 keV $\gamma$-rays. 45
3.4 a) $\gamma$-ray spectrum of the mass $A = 129$ in delayed coincidence with the fission fragments. b) Si(Li) spectrum obtained in coincidence with the $\gamma$-rays of 359.0, 995.2 and 1354.1 keV. c) Time spectrum of 333.8 keV. . . . . 47
3.5 $\gamma - \gamma$ coincidences between the four transitions of the isomeric cascade observed in $^{129}$In. . . . . 48
3.6 Time spectrum of $^{126,128,130}$In. . . . . 49
3.7 Predicted fission yields for In and Cd isotopes provided by Prof. Rubchenya. . . . . 50
3.8 a) Germanium spectrum obtained in delayed coincidence with mass $A = 125$. b) Time spectrum of $^{125}$Cd. . . . . 51
3.9 Experimental levels of $^{125}$Cd in comparison with experimental levels of $^{123}$Cd and a theoretical calculation on $^{127}$Cd. The energies are given in keV. . . . . 52

3.10 Level schemes of $^{123,125,127,129}$In. The level energies (keV) in parenthesis are deduced from $\beta$ spectra [6] and have large uncertainties. . . . . 53

4.1 Calculated yrast states in $^{129}$In. . . . . 61
4.2 Experimental and calculated energies in keV for $^{129}$In and $^{130}$Sn (a) and for $^{127}$In and $^{128}$Sn (b). . . . . 62
4.3 Calculated yrast states in $^{127}$In. . . . . 63
4.4 Experimental and calculated energies in keV for the odd-odd In. . . . . 66
4.5 Experimental and calculated energies in keV for $^{126,128}$Cd. . . 69
4.6 Experimental and calculated energies in keV for $^{204}$Hg [52] and $^{128}$Cd. . . . . 70
4.7 Calculated levels, transition probabilities and lifetime of $^{130}$Cd. The energies are in keV. . . . . 71
4.8 Experimental levels of $^{125}$Cd in comparison with a theoretical calculation of $^{127}$Cd. The energies are in keV. . . . . 73

# List of Tables


3.1 Relative intensities of the transitions observed in $^{123}$In . . . . . 43
3.2 Calculated K over L ratios for a transition of 47 keV in $^{127}$In . 44
3.3 Relative intensities of the transitions observed in $^{129}$In . . . . . 46
3.4 Half-lives measured in the present work along with the already known values. . . . . 55

4.1 Single particle energies used in the calculation. . . . . 58
4.2 Amplitudes in % of the main configurations contributing to the wave functions of the $9/2^+$, $11/2^+$, $13/2^+$, $17/2^-$, $23/2^-$ and $29/2^+$ levels of $^{129}$In. Only the amplitudes bigger than 1% are reported. . . . . 60
4.3 Amplitudes in % of the main configurations contributing to the wave functions of the $9/2^+$, $11/2^+$, $13/2^+$, $25/2^+$, $29/2^+$ and $15/2^-$, $17/2^-$, $19/2^-$, $21/2^-$ and $23/2^-$ levels of $^{127}$In. Only the amplitudes bigger than 10% are reported. . . . . 64
4.4 Amplitude of the main configurations contributing to the wave functions of the $1^-$ and $3^+$ states in $^{130,128}$In. Only the amplitudes bigger than 2% are reported. . . . . 67
4.5 Experimental $B(M2)$ and $B(E3)$ values of $M2/E3$ transitions in $^{125,126,128,129,130}$In [32, 33] and $^{123,125,127,129}$Sn [6, 51]. The $B(M2)$ and $B(E3)$ values reported are obtained assuming no admixture of the multipolarities. In the indium isotopes the transitions have predominantly an $M2$ character, whereas in the tin isotopes it is not possible to exclude an $E3$ component, as discussed in the text. . . . . 68
4.6 Amplitudes in % of the main configurations contributing to the wave functions of the $0^+$, $2^+$, $4^+$, $6^+$ and $8^+$ and levels of $^{130,128}$Cd. Only the amplitudes bigger than 6% are reported. . 72

# Introduction

The structure of magic or semi-magic nuclei is dominated by the single particle degree of freedom and shell effects. On the neutron-rich side of the nuclear landscape above $^{48}$Ca, the only doubly magic unstable nuclei experimentally accessible at present are $^{132}$Sn and $^{78}$Ni. The study of these nuclei and their neighbors is of special interest, as shown by the attention given to them in recent papers, e.g. [1–3]. Indeed, obtaining new experimental information offers a unique opportunity to test the basic ingredients of the nuclear shell model, such as the residual interaction, far away from stability, and to detect any departures from the shell model.

In this work the attention was focussed on In and Cd isotopes in the mass range $A = 123$ to 130, in the vicinity of $^{132}$Sn. Measurements in these nuclei are an experimental challenge because they are very difficult to produce, therefore the experimental information is very scarce up to now. The nuclear structure picture is more complete for nuclei above the $Z$=50 shell-closure [1], for instance, Sb and Te isotopes, which are much easier to produce. Only recently, Kautzsch *et al.* [3] have obtained some spectroscopic information on $^{126,128}$Cd, which have two proton and two and four neutron holes respectively, inside the $^{132}$Sn core. Although this information is still rather scarce, it seems to indicate that these nuclei exhibit some degree of collectivity. The authors of [3] take this effect as plausible evidence for a weakening of the shell structure. This is one of the main motivations to carry out a study of the neutron-rich In and Cd nuclei. A very broad spectrum of complementary techniques is currently used to investigate the structure of neutron-rich nuclei in the region, among them the search for $\mu$s isomers and the study of their decay schemes are very powerful tools, as the isomers are very abundant in the vicinity of $^{132}$Sn [1]. The isomerism originates in the extra binding energy gained by high-spin states from the large overlap of the proton and neutron orbitals occupied by the valence particle or holes,

in particular in the stretched coupling. This effect makes the yrast line very irregular, therefore some states can only decay by low-energy or high-multipolarity transitions, giving rise to isomers. In the region of the doubly magic $^{132}$Sn a very important role is played by the unique parity states $\pi g_{9/2}$ and $\nu h_{11/2}$, both close to the Fermi level.

In the present work we searched for and studied the decay of $\mu$s isomers in the neutron-rich mass $A$=123 to 130 nuclei with the LOHENGRIN spectrometer at the ILL reactor in Grenoble. The aim was to complete the previous data on the heavy Cd and In isotopes. Apart from the above quoted study on the Cd isotopes, the low-spin levels up to $13/2\hbar$ in $^{123-127}$In were previously investigated from the $\beta$-decay of Cd isotopes [4, 5] and, very recently, high-spin ms isomers in $^{125-129}$In were discovered [6, 7]. Preliminary reports were also presented by M. Hellström *et al.* [8, 9] on the search for $\mu$s isomers in the heavy Cd and In isotopes at the FRS spectrometer at GSI, but no level schemes were proposed.

Motivated by the new data obtained from the present experiments, theoretical calculations were performed to test the ability of the shell model to describe the heavy Cd and In isotopes, with proton and neutron holes inside the $^{132}$Sn core. A realistic effective interaction derived from the CD-Bonn nucleon-nucleon potential [10] was used. Similar calculations were performed in [11, 12] for nuclei with proton particles and neutron holes around $^{132}$Sn. A very good agreement with the experimental data was found.

In the first chapter the motivations of this work are discussed, and the main theoretical concepts used in the work are introduced. In the second chapter the experimental technique is described, and the experimental results obtained are reported in the third chapter. The fourth chapter contains a brief description of the shell-model calculation performed in this work, and the comparison between experiment and theory is discussed.

# Chapter 1

# Motivation and theoretical background

Most of our knowledge of nuclei comes from investigations near the valley of stability or on the proton rich side of the nuclear landscape. This is natural because beams and targets used in accelerators are stable and therefore the nuclei produced in reactions are near stability or proton-rich simply because they result from fusion reactions. The neutron-rich side of the nuclear landscape is largely unknown, even the position of the neutron drip line, the limit of existence of a nucleus with respect to the strong interaction, is highly uncertain. Access to spectroscopic information on weakly bound nuclei with high, relative to stability, $N/Z$ ratio, is extremely intriguing because we genuinely believe that new aspects of nuclear physics are waiting to manifest themselves.

One hypothesis to test is the weakening of the shell gaps (shell quenching) for very neutron-rich nuclei. The first request a nuclear potential must fulfill is the capability to reproduce the magic numbers 2, 8, 20, 28, 50, 82 etc... All the modelling of the nuclear potential is made keeping that well in mind. The nuclear interaction far away from stability could be very different from the ones shaped on the basis of observations in nearly stable nuclei, reflecting changes in the structure due to a high neutron to proton ratio. The shell gaps we are used to, can therefore disappear or change. Different scenarios can be depicted, depending on the interaction used for the calculation, but in absence of experimental information they have to be considered speculative. Moreover, the abundance of the elements heavier than iron in the universe seems to be influenced by the explosion of supernovae, the site where the

r-process (rapid neutron capture) is suspected to take place. It consists of the rapid capture, with respect to $\beta$-decay, of several neutrons by a stable nucleus, until a "waiting point" nucleus is reached and the very neutron-rich nuclei formed start to $\beta$-decay toward stability. The waiting-point nuclei are characterized by low cross sections for neutron capture, hence the neutron capture does not take place anymore. The nuclei involved in the r-process lie of course on the neutron-rich side of the nuclear landscape, therefore a more extended knowledge of this region is essential also for nuclear astrophysics. It is not necessary, however, to go to the drip line to obtain critical new information, indeed in many mass regions even the first unstable neutron-rich nuclei are little, if at all, studied. This is the case in some of the heavy ($A \geq 123$) indium and cadmium isotopes explored in this work using neutron-induced fission reactions. Fission reactions are currently used to produce neutron-rich nuclei, in particular in two mass regions, $A \sim 100$ and the vicinity of $^{132}$Sn considered here. The nucleus $^{132}$Sn, which has 50 protons and 82 neutrons, lives for about 40 seconds after its production. It has a magic number of both neutrons and protons making it a very rigid spherical nuclear system and a benchmark for nuclear structure investigations. The properties of its neighbors, with few particles (or holes) added to the closed core, are predominantly determined by these very active additional particles (holes). It is very important to note that such nuclei are sufficiently simple to be reliably modeled (although at the limit) by the state-of-the-art nuclear structure model calculations. Thus if there is good quality experimental information on these nuclei, it provides means for a very rigorous examination of our current understanding of exotic nuclear systems via a comparison of theoretical predictions and experimental results. The nuclei slightly more complex than $^{132}$Sn have the unique ability to provide the first hint on what happens when many more neutrons or protons are added, something nothing is known about at present. One should note that nuclei which have a substantial number of extra neutrons and protons above or below $^{132}$Sn are too complex to serve as rigorous tests, as they have too many possible interactions between the active particles and current theoretical models cannot handle such cases with high precision. In this chapter a description of the region under study and an overview the theoretical concepts applied in the following is given.

## 1.1 The region of $^{132}$Sn

$^{132}$Sn is a doubly magic nucleus ($Z = 50$, $N = 82$) lying in the neutron-rich side of the nuclear landscape. These facts make the study of this nucleus and its neighbors interesting, as already discussed in the introduction of this chapter. Several techniques are currently used to investigate the nuclear structure of the neutron-rich nuclei in the vicinity of $^{132}$Sn, among them the search for $\mu$s isomers is a very powerful tool, the isomers being very abundant in the region. In figure 1.1 the known microsecond isomers in the region are shown, including the ones found in this work.

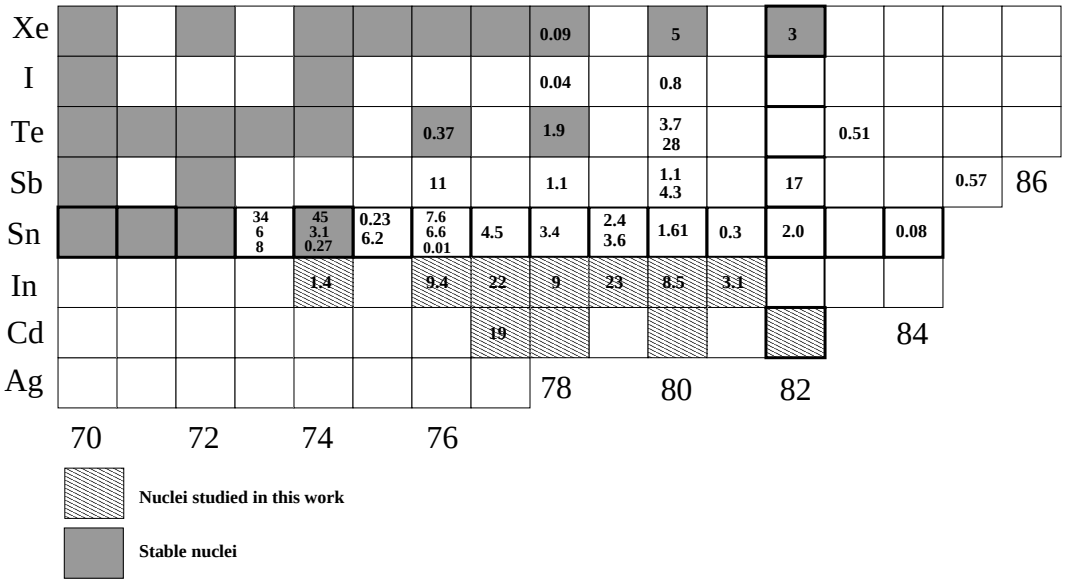


Figure 1.1: Microseconds isomers in the vicinity of $^{132}$Sn. The half-lives indicated are in $\mu$s.

The experimental information available are more complete for nuclei with $Z \geq 50$, Sn, Sb and Te isotopes for example, than in indium and cadmium isotopes ($Z < 50$) which are very difficult to produce. In the latter nuclei the presence of two high-spin states at low excitation energy as the $\pi g_{9/2}$ and $\nu h_{11/2}$ and the very strong $p-n$ interaction in the $(\pi g_{9/2}^{-1} \nu h_{11/2}^{-1})$ configuration are expected to make the yrast line very perturbed. Such irregularities can

give rise to long-lived high-spin isomers. They are mainly high-spin yrast traps which decay to states close to the yrast line.
Evidence of isomerism in the region was presented by M. Hellström *et al.*, [8, 9] but no level schemes were proposed. Very recently, the onset of collectivity in heavy Cd isotopes ($^{126,128}$Cd) was found [3], and the authors proposed the weakening of the shell structure as possible interpretation of the experimental findings. Moreover, the path of the rapid neutron capture process (r-process) is thought to pass through $^{130}$Cd, which is expected to have a $\mu$s isomer in the $8^+$ state. The relevance for astrophysics, along with the unresolved question about the weakening of the shell structure spurred us to investigate extensively the region of heavy ($A \geq 123$) Cd and In isotopes at the ILL reactor in Grenoble using the LOHENGRIN separator [13] and $\gamma$-rays spectroscopy.

## 1.2 Nuclear Isomers

In the literature, a nucleus is considered to be in an isomeric state when its lifetime is long compared with the lifetime of the neighboring states. This definition obviously lacks of precision, and the question arises: what does "long" mean?. It is impossible to indicate a value of the lifetime after which a state is an isomer, but states whose lifetimes are of the order of some ns can be definitely considered isomeric. Nuclear isomers have been identified in many nuclei throughout the periodic table. O. Hahn, co-discoverer with Lise Meitner of nuclear fission phenomenon, is credited with the discovery of nuclear isomerism in 1921 [14], and its interpretation in terms of inhibited gamma decay was provided by Weizsäcker in 1936 [15]. Since that early time, nuclear isomers have drawn a lot of attention because their lifetimes are relatively easy to measure, hence information essential to the understanding of the nuclear structure, such as transition probabilities, can be deduced. It should be mentioned that now other techniques, such as Doppler Shift Attenuation Method, Plunger, Centroid Shift etc.. are available to measure short lifetimes. In addition, isomeric states have often simple configurations, offering a unique tool to test the basic ingredients of theoretical models as the shell model. Let us now see in more details how to calculate the lifetime of an excited state. The partial lifetime of a state is inversely proportional to the probability $P_\gamma$ that the initial state of energy $E_i$ and spin $I_i$ decays into the final state of energy $E_f$ and spin $I_f$ by emission of a photon $\gamma$ of

energy $E_\gamma = \hbar\omega = E_f - E_i$. If the matrix elements of the interaction $H$ responsible for the transition are known the following expression for $P_\gamma$ [16] can be evaluated:

$$P_\gamma(\sigma L; I_i \to I_f) = \frac{8\pi(L+1)}{\hbar L[(2L+1)!!]^2}(\frac{\omega}{c})^{2L+1} B(\sigma L; I_i \to I_f), \tag{1.1}$$

with

$$\begin{aligned} B(\sigma L; I_i \to I_f) &= \Sigma_{M,M_f} | < I_f M_f | H(\sigma L, M) | I_i M_i > |^2 \\ &= (2I_i+1)^{-1} | < I_f || H(\sigma L) || I_i > |^2, \end{aligned} \tag{1.2}$$

where $\sigma$ is the character of the transition (magnetic or electric) and $L$ the multipolarity of the transition. Along with the emission of a $\gamma$-ray, an excited state can de-excites via the emission of an electron. For more detail on this phenomenon see section 1.4. The probability $P_{e^-}$ of emission of an electron is proportional to the probability $P_\gamma$ of emission of a $\gamma$-ray by the total conversion coefficient $\alpha_T$. The total probability that the initial state decays to the final state is then:

$$P = P_{e^-} + P_\gamma = P_\gamma(1 + \alpha_T). \tag{1.3}$$

Equation 1.3 leads directly to the lifetime of a state $\tau = 1/P$. From 1.1 and 1.3 it is clear that the quantities important in determining the lifetime of a state are the multipolarity $L$ of the transition, its energy $\hbar\omega$, and the reduced matrix element $B(\sigma L; I_i \to I_f)$. These quantities are at the origin of the different type of isomers in nuclei.

### 1.2.1 Spin isomers

The higher the multipolarity of a transition the longer its lifetime. This phenomenon is called spin isomerism. High multipolarity implies a big change in the spin during the transition, therefore it is the big difference in the spins of the initial and final state that causes the long lifetime. An example is the $7^-$ state of $^{198}$Tl, which decays in 1.87 h to the $3^-$ state with an $M4$ transition of 261 keV.

### 1.2.2 Shape isomers

In some cases, the potential energy of a nucleus can have more than one minimum (see fig. 1.2) and, once the nucleus lies in this second minimum, it can only de-excites passing through the potential barrier (tunnelling effect) or fissioning.

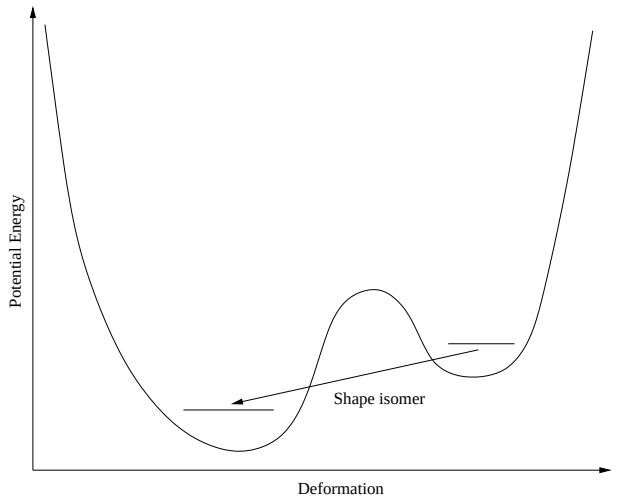


Figure 1.2: Potential energy versus deformation in the case of the existence of a second minimum

The shape of the nucleus in these two states is substantially different, hence the overlapping of the final and initial wave functions via the $H$ operator is not big, causing the isomer. An example of shape isomer is the super deformed $0^+$ state of $^{238}$U, which decays to another $0^+$ deformed state, the ground state, with a transition of 225 ns.

### 1.2.3 K isomers

The projection $K$ of the angular momentum on the symmetry axis of a deformed nucleus appears to be approximately conserved, as illustrated by the existence of isomeric states in many nuclei in the mass 180 region [17]. Electromagnetic transitions must obey the K-selection rule, $\Delta K \leq L$, where $L$ is the multipolarity of the transition and $\Delta K$ the variation of the $K$ quantum number, if $K$ is a good quantum number as in axial symmetric nuclei. Several

studies have shown that highly $K$-forbidden transitions are hindered rather than strictly forbidden, and the hindrance factor is strongly correlated with the degree of forbiddenness $\nu = \Delta K - L$, implying partial breakdown of the $K$-selection rule. In this case the transition is not favored and the lifetime is long. An example of a $K$ isomer is $^{182}$Os [18], where a $K = 25^+$ isomeric state decays by a single gamma-ray transition to a collective yrast state with $K = 0$. This transition should be highly hindered because it changes $K$ by 25 units, while only changing spin by 1 unit. However, the half life of the isomer is only 130 ns.

### 1.2.4 Isomers due to low transition energy

From equation 1.1 it is clear that the smaller the energy of the transition the longer is the lifetime. An example is the $2^+$ state of $^{154}$Sm, which decays by an $E2$ transition of 82 keV with a lifetime of 3 ns. When two effects are combined, low energy and high multipolarity, the lifetime of the initial state can become considerably long. This type of transition can be highly converted, therefore the measurement of conversion electrons becomes extremely important.

## 1.3 Weisskopf estimations for the lifetimes

The expressions 1.1 and 1.3 which give the lifetime of an excited state are not easy to evaluate, because knowledge of the interaction matrix elements is necessary. In order to have a somewhat simpler unit for comparison with observed $\gamma$ lifetimes the most common method used is the Weisskopf approximation [16]. The two type of transition (electric and magnetic) are treated differently, according with the different moment associated with magnetic and electric multipole. The wave functions are approximated by a constant extending out to the radius $R = 1.2\ A^{\frac{1}{3}}$ fm [16], and the transition is considered to have a single particle character, taking place between two states of spin $L + 1/2$ and $1/2$ respectively. Making these assumptions, the two following expressions for the transition probability $\lambda(\sigma L)$ can be derived:

$$\lambda(EL) = \frac{4.4(L+1)}{L[(2L+1)!!]^2}\left(\frac{3}{L+3}\right)^2\left(\frac{E_\gamma}{197}\right)^{2L+1} R^{2L} \times 10^{21} s^{-1}, \qquad (1.4)$$

$$\lambda(ML) = \frac{1.9(L+1)}{L[(2L+1)!!]^2}\left(\frac{3}{L+3}\right)^2\left(\frac{E_\gamma}{197}\right)^{2L+1} R^{2L-2} \times 10^{21} s^{-1}, \quad (1.5)$$

with $E_\gamma$ in MeV and $R$ in fm. One has to keep in mind that these useful formulae are obtained making rough simplifications, but surprisingly in several cases they work, and considering the decay of the excited state as a single particle process, which is not always the case. They essentially give the order of magnitude of the transition probabilities for the various multipolarities, in cases where the behavior of the nucleus is not collective. The transition probabilities are often expressed in Weisskopf units (W.u.), it means that the experimental (or theoretical) values are divided by the values obtained in the Weisskopf approximation. The aim is to have a feeling about the character of the transition (single particle or collective) and its hindrance.

## 1.4 Conversion electrons

A nucleus in an excited state can perform a transition to a lower state not only by emitting a light quantum, but also transmitting energy directly to the electrons surrounding it. The transition is then connected with the ejection of an atomic electron from a bound orbit. This process is called internal conversion [19]. The transmission of energy to the electrons occurs independently of the emission of a light quantum, in other words, it does not result from the absorption by the electrons surrounding the nucleus of the light quantum emitted by the nucleus itself. Such an internal photoelectric effect has a negligible probability to occur. The kinetic energy $E_{e^-}$ of the emitted electron is:

$$E_{e^-} = \Delta E - B_{e^-} \quad (1.6)$$

where $\Delta E$ is the energy difference between the initial and the final state and $B_{e^-}$ is the electron binding energy. The ratio between the probability of emission of an electron from any atomic shell and the probability of emission of a photon is called total conversion coefficient $\alpha_T$. It is more useful sometimes to consider the partial conversion coefficients $\alpha_K$, $\alpha_L$, $\alpha_M$ etc.. relative to the electron emitted from the $K$, $L$, and $M$ etc.. shells respectively. Obviously the total conversion coefficient is just the sum of all the partial conversion

coefficients. The main features of the process can be understood qualitatively making a simple non relativistic calculation, considering a plane wave for the outgoing electron. The result is the following:

$$\begin{cases} \alpha_T = Z^3 e^8 \frac{L}{L+1} \left(\frac{2}{\omega}\right)^{L+5/2} \frac{1}{n^3} & \text{for electric transition} \\ \alpha_T = Z^3 e^8 \left(\frac{2}{\omega}\right)^{L+3/2} \frac{1}{n^3} & \text{for magnetic transition} \end{cases}, \qquad (1.7)$$

where $Z$ is the nuclear proton number, $e$ is the electron charge, $n$ is the principal quantum number and $\omega$ the energy of the photon emitted in competition with the electron. From eq. 1.7 it is clear that:

- the conversion is large for small $\omega$ and decreases rapidly for larger values of $\omega$
- the conversion coefficient increases with increasing the multipole order $L$
- the conversion coefficient is maximum for $K$ electrons, being the ratios $K/L$ and $L/M$ approximately 8 and 3 respectively. The $K/L$ $L/M$ etc.. ratios depend on the multipolarity of the transition

These features make conversion electrons measurements a very useful tool to get spectroscopic information in case of low-energy isomeric transitions. Indeed in this case the rate of electrons can be comparable or even higher than the rate of $\gamma$-rays, and, if both electrons and $\gamma$-rays are measured, the multipolarity of the converted transition can be established. The knowledge of the multipolarity and the lifetime allow not only the level scheme to be built, but also the transition probabilities to be evaluated.

## 1.5 The shell model

The nuclei under study have few holes inside the closed core $^{132}$Sn, therefore they have been studied in the framework of the nuclear shell model, whose main features are explained in the following. The basic assumption in the nuclear shell model is that, to the first order, each nucleon is moving independently in an average field. The total Hamiltonian $H_0$ of the system can therefore be written as sum of the Hamiltonians $h_i$ of the single components of the nucleus:

$$H_0 = \sum_{i=1}^{A} h_i = \sum_{i=1}^{A} (T_i + U_i), \tag{1.8}$$

where $T_i$ and $U_i$ are the kinetic energy and the average field potential energy for each of the $A$ nucleons. The single particle wave functions $\phi_a$ are solution of the one body Schrödinger equation:

$$h_i \phi_a = \epsilon_a \phi_a, \tag{1.9}$$

where $\epsilon_a$ are the single particles energies. The total wave function of the $A$-body system is the antisymmetrised product (Slater determinant) of single particle wave functions solution of eq. 1.9:

$$\psi_{a_1 \ldots\ldots a_A}(i = 1, \ldots\ldots, A) = \frac{1}{\sqrt{A!}} \begin{vmatrix} \phi_{a_1}(1) & \phi_{a_1}(2) & \ldots & \phi_{a_1}(A) \\ \phi_{a_2}(1) & \phi_{a_2}(2) & \ldots & \phi_{a_2}(A) \\ \ldots & \ldots & \ldots & \ldots \\ \phi_{a_A}(1) & \phi_{a_A}(2) & \ldots & \phi_{a_A}(A) \end{vmatrix} . \tag{1.10}$$

One of the most used average field is the phenomenological Wood-Saxon potential. For practical reasons, it can be approximated by an harmonic oscillator, plus a centrifugal $l^2$ term, plus an $l \cdot s$ spin-orbit term, in order to reproduce the magic numbers 2, 8, 28, 50, 82, 126 etc... The result is shown in fig. 1.3. In fact, it was the discovery of the magic numbers which lead Mayer and Jensen [20, 21] to the nuclear shell model, by analogy with atomic physics.

The real $A$-nucleon Hamiltonian can be written as:

$$H = \sum_{i=1}^{A} T_i + \frac{1}{2} \sum_{i,j=1}^{A} V_{i,j}, \tag{1.11}$$

where $V_{i,j}$ is the two-body nuclear potential. It is convenient to express this Hamiltonian in terms of the Hamiltonian $H_0$ which describes the independent motion of $A$ nucleons:

$$H = \sum_{i=1}^{A} (T_i + U_i) + \frac{1}{2} \sum_{i,j=1}^{A} V_{i,j} - \sum_{i=1}^{A} U_i = \sum_{i=1}^{A} (T_i + U_i) + H_{res} = H_0 + H_{res} \tag{1.12}$$

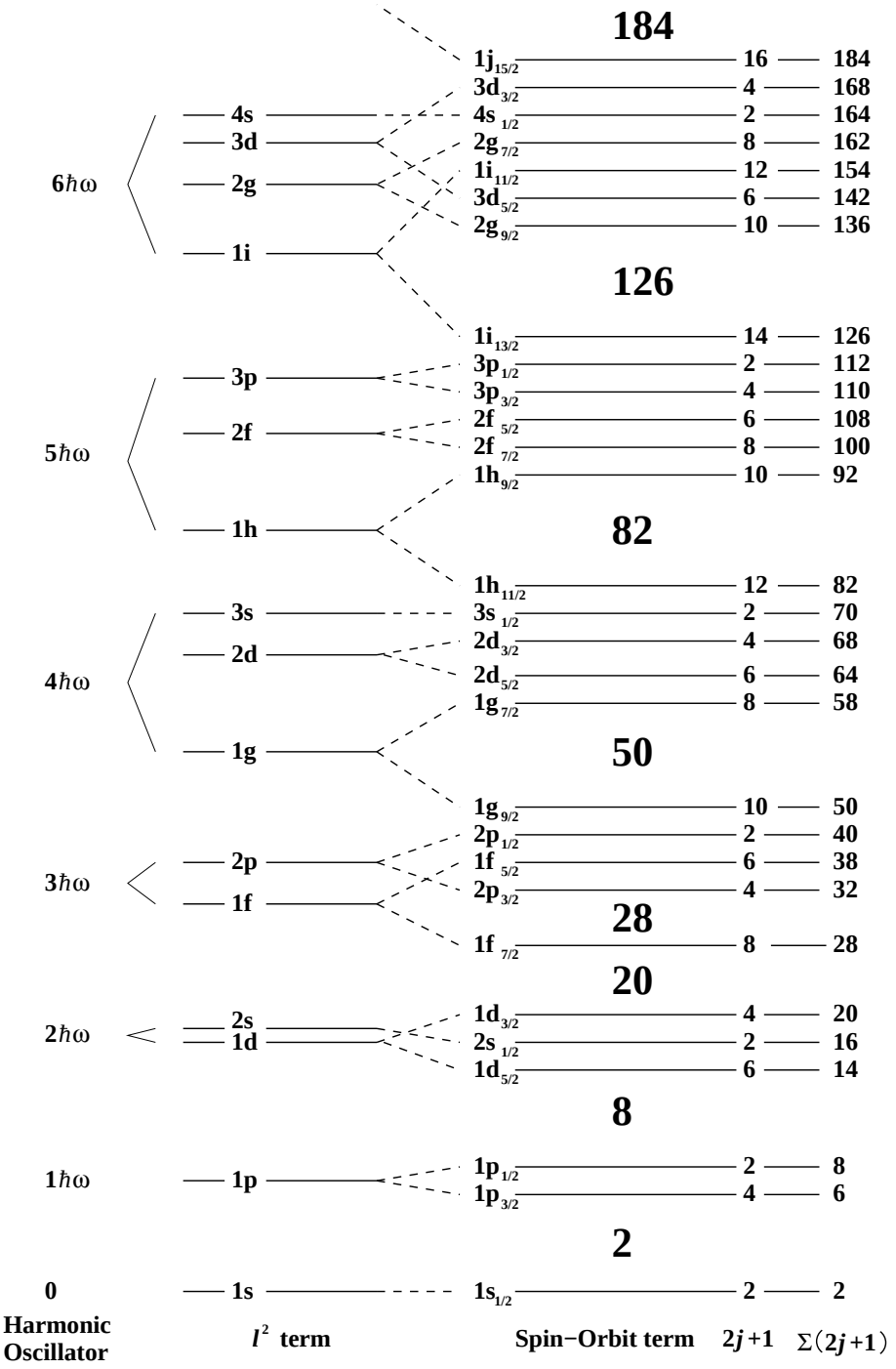


Figure 1.3: Single particle level sequence for an Hamiltonian consisting of a central harmonic oscillator, a centrifugal $l^2$ term and a spin-orbit $l \cdot s$ term, taken from [22].

The residual interaction $H_{res}$ is the most important part of the Hamiltonian, as it determines the structure of a given nucleus. It is impossible for practical calculations to take the full Hilbert space into account, due to the high dimension of the Hamiltonian matrix which becomes impossible to diagonalize. The concept of closed shells helps here, indeed one can assume that only the valence particles (or holes) can move from the orbitals they occupy in the ground state to other orbitals in the same principal shell, drastically reducing the number of orbitals involved in the calculations. This corresponds to an inert core not participating to the excitations. The Hamiltonian turns to an effective operator, and the Schrödinger equation becomes:

$$H_{eff}\psi_{eff} = E\psi_{eff}. \tag{1.13}$$

The wave functions $\psi_{eff}$ are generally a small part of the real wave functions $\psi$, but nevertheless they carry the most part of the properties of the states. The choice of an appropriate residual interaction is a problem difficult to solve. One possible approach is to start from the free nucleon-nucleon interaction and to try to incorporate the necessary modifications to obtain a so-called realistic interaction, able to describe at least the excited states of nuclei with few valence particle (or holes). In this work the Cd-Bonn potential has been used to derive theoretical results [10]. More details on the calculations can be found in section 4.1.

# Chapter 2

# Experimental Technique

High-spin spectroscopy in neutron-rich nuclei represents a formidable experimental challenge. The fusion evaporation reactions which are commonly used to populate high-spin states give rise to evaporation residues which are proton-rich. Therefore, even stable nuclei are, generally, not accessible using the standard in-beam techniques. To produce the neutron-rich nuclei in the vicinity of $^{132}$Sn which we are interested in, one of the best tool is thermal-neutron-induced fission of thick or thin targets. In the latter case, recoil-fragment separators can be used to select in flight the product of interest. The pioneering works using this technique were performed with the spectrometer JOSEF at the reactor FRJ-2 in Jülich [23]. As result, several isomers were discovered, with half-lives ranging between 0.1 $\mu$s and 100 $\mu$s, in the mass regions around $A = 100$ and in the vicinity of $^{132}$Sn. At present, the search for $\mu$s isomers can be performed with three fragment separators: FRS at GSI, LISE3 at GANIL and LOHENGRIN at ILL. Beside the methods used to produce the radioactive beams, the main difference between these facilities is the energy of the nuclei. At FRS, this energy is 700-1000 MeV/nucleon, at LISE3 $\sim$ 60 MeV/nucleon, and less than 1 MeV/nucleon at LOHENGRIN. A high energy, which implies a high velocity, allows a complete $A$ and $Z$ identification of the fragments, while only $A$ identification can be achieved at low energy. The advantage in the latter case is that the fragments can be stopped in a very thin layer of material, without producing secondary reactions, a source of strong background. It is therefore possible to detect the very low-energy $\gamma$-rays or conversion electrons that often de-excite the isomers in the region under study. This is the situation at the LOHENGRIN recoil separator used to carry out the experimental part of this work. In this

chapter the various aspects of the experimental technique used to study $\mu$s isomers in the region around $^{132}$Sn are discussed.

## 2.1 Neutron-induced fission reactions as a tool to produce neutron-rich nuclei

More than fifty years after the discovery of fission its interpretation is still an object of debate. Several models can be used to describe the main features of the process, but none of them is capable, nowadays, of giving a complete and satisfactory picture of it. The aim of this work is *not* to shed light on the fission process, therefore the following discussion is focussed on the aspects of thermal-neutron-induced fission relevant for the $\mu$s isomer experiments in the region below the doubly magic $^{132}$Sn.

Neutron-induced fission is a process in which a neutron is captured by the nucleus of a fissile element and causes it to split, generally into two fragments. The main dynamic phases of the process are summarized in figure 2.1.

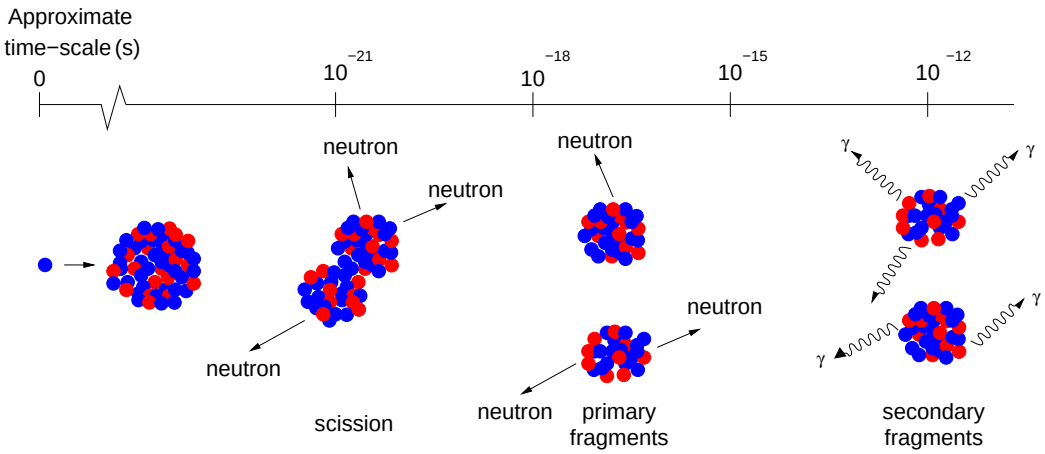


Figure 2.1: A schematic diagram of the neutron-induced fission process with the approximate time-scale on which the phases occur.

After the neutron capture, the compound nucleus (neutron + fissile nucleus) undergoes a rapid transition from a normal nuclear state into a highly deformed configuration which swiftly reaches the point at which it ceases to exist: the *scission point*. Immediately after scission, two high-energy

*primary* fragments separate from each other and begin the process of de-excitation. The primary fragments are so neutron-rich with respect to stable isotopes, that neutron emission is immediately the favored energy-loss mechanism. When neutron emission becomes energetically impossible, the process of $\gamma$-ray decay takes over. At this stage, the fragments are referred to as *secondary* fragments and the $\gamma$ rays which they emit are known as *prompt* $\gamma$ rays. The emission of these prompt $\gamma$ rays eventually leads to a ground state whose lifetime is far greater than the time-scale of the fission process and is therefore, in relative terms, considered to be effectively stable. These radioactive secondary fragments subsequently undergo a series of $\beta$ decays until they transforms themselves into more stable members of the mass chain into which they were born. In some favorable cases the secondary fragments are trapped in yrast states having a relatively long half-life ($\geq 10^{-6}$ s), allowing the experimentalists to use recoil-separators to select them in flight, while they are still in their isomeric states.

Two essential pieces of information are needed to carry out $\gamma$-spectroscopy experiments using beams resulting from fission reaction and a separation process:

- the mass and isotopic yield of the fragments
- the kinetic energy distributions of the fragments

The importance of the first point resides not only in the evaluation of the feasibility of a measurement or in the estimation of the necessary beam-time, but also in the fact that, in some cases, as for example the experiments performed using the LOHENGRIN mass separator, the non-observation of an isomer can lead to an upper limit of its lifetime. The mass yields of fission products of thermal-neutron-induced fission reactions were measured at the LOHENGRIN separator for several fissile targets. The results are reported in fig. 2.2.

It is clear from fig. 2.2 that the region of the nuclear landscape of the nuclei slightly lighter than $^{132}$Sn is difficult to access because the curve of the mass yield has a minimum around $A \sim 120$, the so-called symmetry region, corresponding to the symmetric fission. The reason for that is the essential role played by a closed-shell structure in the formation of the fission fragments, when fission reactions occur at low excitation energy. At some stage of the fission process, the fragments begin to adopt the properties of

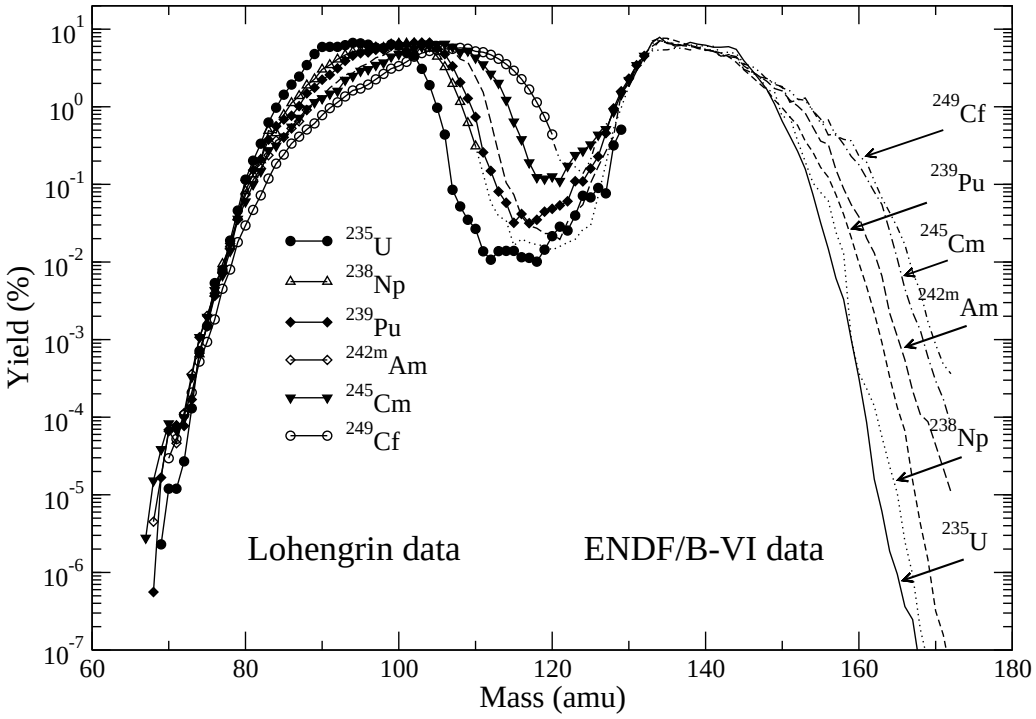


Figure 2.2: Mass yields of fission fragments for thermal-neutron induced fission of $^{235}$U, $^{238}$Np, $^{239}$Pu, $^{242}$Am, $^{245}$Cm and $^{249}$Cf. The data plotted, if existing, are measured at the LOHENGRIN mass separator. To complete the curve, the yields of some heavy masses are taken from the ENDF/B-VI database. Image provided by courtesy of Dr. Igor Tsekhanovich.

individual nuclei and the rapid re-arrangement of nucleon orbitals is governed by the shell model. The shell model has a tendency to prevent the genesis of a fragment that is close to but slightly lighter than $^{132}$Sn, preferring instead to maintain the $Z = 50, N = 82$ shell border and thus creating one fragment slightly heavier than $^{132}$Sn and a much lighter fragment with all the remaining mass. The exact circumstances surrounding how these shell effects occur in the pre-scissioning system are, at present, not fully understood.

The evaluation of isotopic yields at the LOHENGRIN separator, in absence of measured values, was provided by Prof. V. Rubchenya during his collaboration with the ILL institute. A full description of the method can be found in [24] and references therein. For the sake of completeness the model

is briefly described in the following. The yield $Y$ of a specific nucleus of mass $A$ and charge $Z$ is defined as:

$$Y(A,Z) = \sum_n P_n(A+n,Z) P_{pre}(A+n,Z) Y_{pre}(A+n), \qquad (2.1)$$

where $P_n(A+n,Z)$ is the probability of prompt emission of $n$ neutrons from a fragment of mass $A+n$ and charge $Z$, $P_{pre}(A+n,Z)$ is the charge distribution of the $A+n$ isobaric chain, and $Y_{pre}(A+n)$ is the yield of the primary fragment of mass $(A+n)$. $P_{pre}(A+n,Z)$ and $Y_{pre}(A+n)$ can be factorized into two terms, a smoothed distribution $\widetilde{P}$, and a function $\widetilde{Y}$ which describe the odd-even staggering observed at low excitation energy. The core of the model is the choice of the smoothed mass distribution $\widetilde{Y}$. The approach of Brosa [25] based on the multi-modal nature of the fission process was adopted. Within this framework, the pre-scission yield can be considered as the sum of several terms, each of them representing one fission mode:

$$\begin{aligned} Y_{pre}(A) = {} & C_{SY} Y_{SY}(A) + C_{SI} Y_{SI}(A) + C_{SII} Y_{SII}(A) \\ & + C_{SA1} Y_{SA1}(A) + C_{SA2} Y_{SA2}(A), \end{aligned} \qquad (2.2)$$

where $Y_{SY}(A)$ corresponds to the symmetric component, $Y_{SI}(A)$ is connected with the magic numbers $Z = 50$ and $N = 82$, $Y_{SII}(A)$ is connected with the nuclear shell $N = 86 - 90$, $Y_{SA1}(A)$ and $Y_{SA2}(A)$ are connected with the closed shell $Z = 28$ and $N = 50$. The coefficients $C_i$ in eq. 2.2 were obtained by comparison with LOHENGRIN experimental data. The probability of neutron emission is calculated with a simplified statistical description [26], whereas the average value and variation of the smoothed charge distribution are calculated in the framework of the scission-point model [27].

The second point mentioned above, the knowledge of the kinetic energy distribution of the fission fragments, is crucial for experiments involving nuclei with very low production yields, in order to maximize the number of nuclei in the beam by selecting an appropriate value of the kinetic energy (see next section). The average kinetic energy of the fragments and its distribution has been derived using a model based on a statistical approach [28, 29]. Two main assumptions are made. Firstly, that at the end of the fission process it is possible to define a temperature $T$, directly proportional to the $Q$ value of the reaction, at which the fragments are excited, and secondly, that the fragments are excited independently. The constant which determines the

relationship between $T$ and $Q$ is found to be independent of the fissioning system [28]. Once the temperature of the compound nucleus is determined , the following expression for the average total excitation energy $< TXE >$ and the average total kinetic energy $< TKE >$ can be derived:

$$\begin{aligned} < TXE > &= (a_1 + a_2)T^2 \\ < TKE > &= Q + \epsilon - < TXE > \end{aligned} \tag{2.3}$$

where $\epsilon$ is the neutron binding-energy, and $a_1$, $a_2$ are the level density parameters of the two fragments respectively. The average total kinetic energy is distributed onto the average kinetic energies $< E^1_{KIN} >$ and $< E^2_{KIN} >$ of the two fragments of mass $A1$ and $A2$ according to the conservation of energy and momentum:

$$\begin{aligned} < E^1_{KIN} > &= \frac{< TKE >}{1 + \frac{A1}{A2}} \\ < E^2_{KIN} > &= \frac{< TKE >}{1 + \frac{A2}{A1}} \end{aligned} \tag{2.4}$$

The distribution $P(E^*_{1,2})$ of the excitation energy $E^*_{1,2}$ of the two fragments is Maxwell-Boltzmann type:

$$P(E^*_{1,2}) = \frac{1}{N}\rho(E^*_{1,2})e^{-E^*_{1,2}/T}, \tag{2.5}$$

where $N$ is a normalization factor, and $\rho$ is the level density. In the literature several expressions exist for the level density, here one based on the Fermi-gas description is adopted [30]. The distributions of $E^1_{KIN}$ and $E^2_{KIN}$ can be obtained using a Monte-Carlo technique. Four random numbers are generated for $E^*_1$, $E^*_2$, $P(E^*_1)$ and $P(E^*_2)$. If these number fall in the allowed region below the distribution 2.5, the spectra of $E^1_{KIN}$ and $E^2_{KIN}$ are incremented, accordingly with:

$$
\begin{aligned}
E_1^* + E_2^* &= TXE \\
TKE &= Q + \epsilon - TXE \\
E_{KIN}^1 &= \frac{TKE}{1 + \frac{A1}{A2}} \\
E_{KIN}^2 &= \frac{TKE}{1 + \frac{A2}{A1}}
\end{aligned} \tag{2.6}
$$

The neutron evaporation from the primary fragments is taken into account and is calculated with the code PACE II [31]. The comparison between the kinetic-energy distribution obtained with this model and the experimental LOHENGRIN data reported in [28, 29] shows a good agreement.

In this work, two different targets have been used to produce neutron-rich indium and cadmium isotopes, $^{239}$Pu and $^{241}$Pu. The choice of these elements was made considering their high cross-section for neutron capture ($\sim$ 1000 b) and the high production yield of the nuclei under study. Moreover, $^{239,241}$Pu have a high neutron/proton ratio compared to the normally used $^{235,233}$U, and then, hopefully, the production of neutron-rich nuclei is favored. This is especially true for $^{241}$Pu, as confirmed by the results of this work [32, 33]

## 2.2 The LOHENGRIN mass separator

LOHENGRIN [13] is a mass separator of fission fragments recoiling from thin targets placed very close to the core of the high-flux ($5\times10^{14}$ neutron$\times$cm$^{-2}\times$s$^{-1}$) reactor at the Institut Laue-Langevin (ILL) in Grenoble. It consist of a main magnet and a condenser, which together are responsible for the separation of the fission fragments having different ratios $A/q$ and $E/q$ into different parabolas, and a second magnet which focuses the beam. $A$, $E$ and $q$ are the mass, the kinetic energy and the ionic charge of the fragment respectively. In figure 2.3 a picture of the LOHENGRIN separator and its schematic view are shown.

The combined action of a magnetic field $B$, from the main magnet, constant and perpendicular to the velocity, and a constant radial electric field, from the condenser $\mathcal{E}$, on a charged particle moving with a velocity $v$ is described by the following equations:

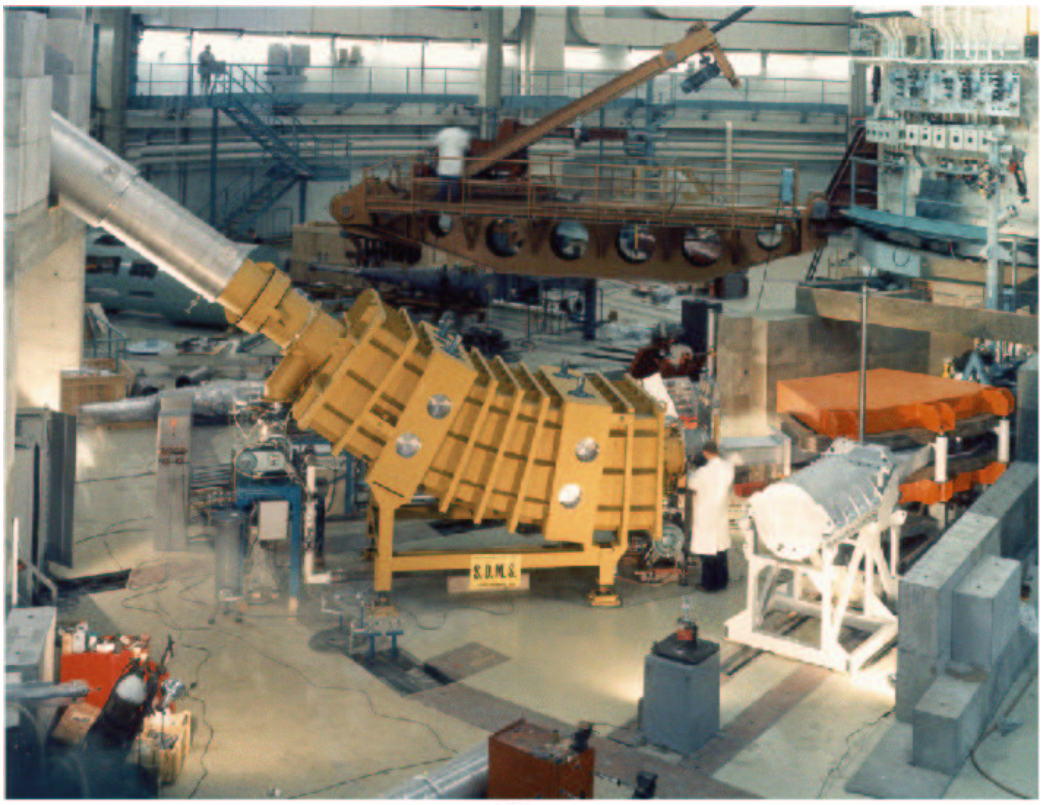

a

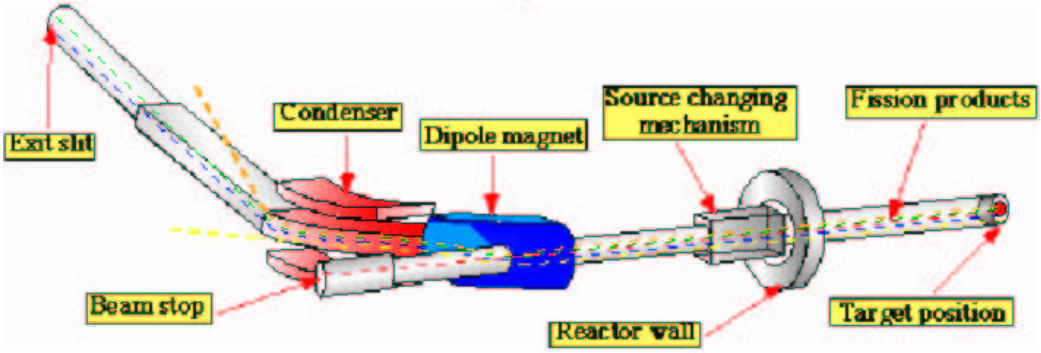


b

Figure 2.3: a) Picture of the LOHENGRIN mass separator. b) Schematic view of the LOHENGRIN mass separator.

$$qvB = \frac{Av^2}{R_m}, \tag{2.7}$$

$$q\mathcal{E} = \frac{Av^2}{R_e}, \tag{2.8}$$

$R_m$ and $R_e$ being the radii of the circular orbits induced by $B$ and $\mathcal{E}$ respectively. Dividing eq. 2.7 by eq. 2.8, an expression for the velocity $v$ can be obtained:

$$v = \frac{\mathcal{E}R_e}{BR_m}. \tag{2.9}$$

The electric field in the region between the plates of a condenser is:

$$\mathcal{E} = \frac{U}{d}, \tag{2.10}$$

where $d$ is the distance between the plates and $U$ the potential. Writing the kinetic energy of an ion of mass-number $A$ in the usual way:

$$E = \frac{1}{2}Av^2, \tag{2.11}$$

and combining equations 2.11, 2.10, 2.9, 2.8 and 2.7, the following expressions can be derived:

$$\frac{A}{q} = \frac{1}{\chi}\frac{B^2}{U}, \qquad \frac{E}{q} = \phi U, \tag{2.12}$$

with:

$$\phi = \frac{R_e}{2d}, \qquad \chi = \frac{2\phi}{R_m^2}. \tag{2.13}$$

The two constants $\phi$ and $\chi$ defined in 2.13 depend only on the characteristics of the separator, and are optimized in order to get the highest possible yield in the focal point every time a new fissile target is used. The values of the electric potential and the magnetic field are chosen to select fragments of the desired mass $A$, kinetic energy $E$ and ionic charge $q$.

The equation of the parabola describing the trajectory of the ions can be obtained considering that the deviations $\Delta y$ along the $y$ axes due to

the electric field, and $\Delta x$ along the $x$ axes due to the magnetic field are proportional to the inverse of the radii $R_e$ and $R_m$:

$$\Delta y \propto \frac{1}{R_e} = \frac{1}{2d\phi}, \qquad \Delta x \propto \frac{1}{R_m} = \left(\frac{\chi}{2\phi}\right)^{1/2}. \tag{2.14}$$

Equations and 2.13 and 2.14 lead to:

$$\Delta y \propto \left(\frac{\mathcal{E}}{B^2}\frac{A}{q}\right)\Delta x^2. \tag{2.15}$$

The energy dispersion in the vertical direction is 7.2 cm for a difference of 1% in the kinetic energy, and the mass dispersion in the horizontal direction is 3.2 cm for a difference of 1% in the mass $A$ of the ions. To improve the mass resolution of the separator one collimator is placed immediately after the target, to reduce the transmission solid angle, and another one is positioned at the exit of the separation system (main magnet + condenser). Additionally, behind the focal point there are nine shutters perpendicular to the collimators to reduce the energy dispersion. A Reverse Energy Dispersion (RED) dipole magnet is used to increase by up to a factor of seven the particle density at the focal position, and to strongly reduce the background. The RED-magnet focuses a section of 40 cm along the vertical direction. This corresponds to an energy range of $\pm$ 2.7 % about the central value.

The flight-time through the separator is of the order of 2 $\mu$s, then the lower limit for the observable lifetimes of excited states is about 0.5 $\mu$s.

After the separation process a beam of fission fragments with a well defined $A/q$ and $E/q$ ratio reaches the focal point. From eq. 2.12 the following expression can be derived:

$$\left(\frac{A}{q}\right)\cdot\left(\frac{E}{q}\right) = \frac{B^2\phi}{\chi}. \tag{2.16}$$

Once the two constants $\phi$ and $\chi$ and the magnetic field $B$ are fixed, all the nuclei of mass $A'$, ionic charge $q'$ and kinetic energy $E'$ with:

$$\left(\frac{A}{q}\right)\cdot\left(\frac{E}{q}\right) = \left(\frac{A'}{q'}\right)\cdot\left(\frac{E'}{q'}\right), \tag{2.17}$$

are focussed in the same region, hence all the ions with mass, kinetic energy and ionic charge satisfying 2.17 contaminate the selected beam. An example of a $\Delta$E spectrum is shown in fig. 2.4, where $\Delta$E is the energy lost by the ions

entering the ionization chamber used during the experiments and described in the next section.

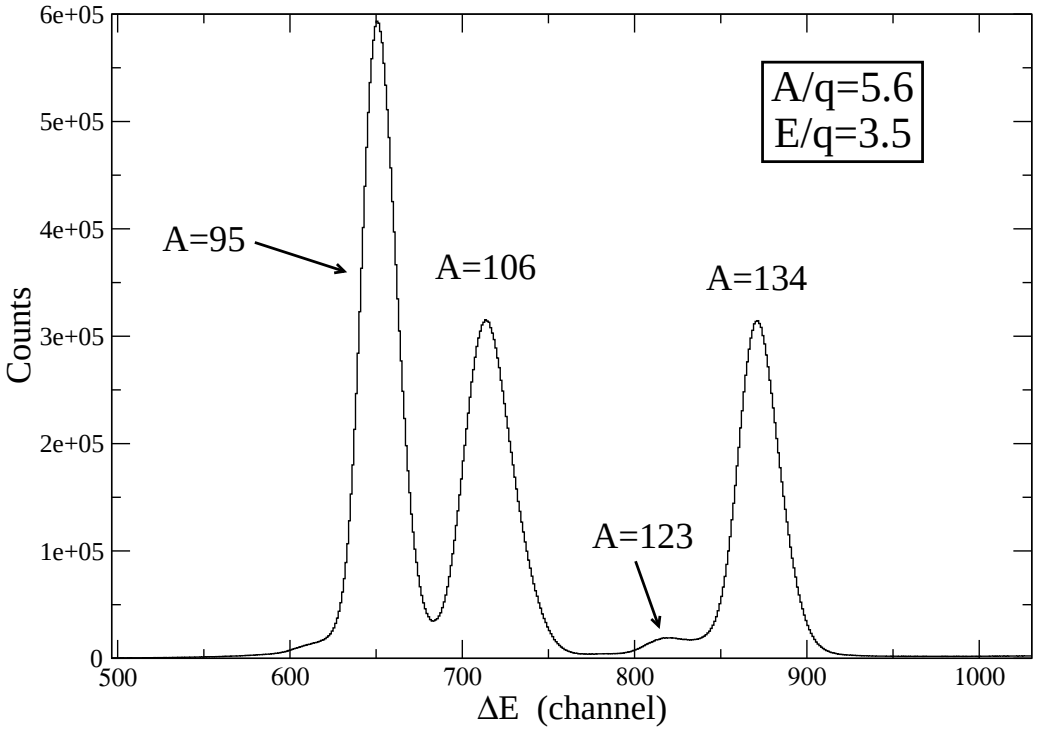


Figure 2.4: ΔE spectrum of the ions entering the ionization chamber. The LOHENGRIN separator was optimized for mass 123.

The values of $E$ and $q$ are chosen to maximize the yield of the nuclei under study. The ionic charge is formed at the passage of the fragments through the target and the nickel foil which surrounds it, due to an exchange of electrons between the fragments and those materials. The average value of the ionic charge in the symmetry region is measured to be 22 at LOHENGRIN. The values of the average kinetic energies of the fragments were estimated using the model described in section 2.1, where no experimental values were available. These values need a correction to account for the energy loss in the target and in the nickel surrounding it. The correction was evaluated using the code SRIM [34].

## 2.3 Experimental set-up

Several experiments have been carried out at the ILL in the last three years to explore the In and Cd region in the vicinity of $^{132}$Sn. Two experimental set-ups both shown in fig. 2.5, have been used. The main difference between set-up 1 and set-up 2 resides in the measurement of conversion electrons, possible only in the first case.

Two experiments devoted to the odd-masses $A = 123, 125, 127, 129$ were performed with set-up 1, measuring both the conversion electrons and $\gamma$-rays. To produce the heaviest of these masses ($A = 129, 127$), a target of $^{241}$Pu of $\sim$ 400 $\mu g/cm^2$ was used. For the others, a target of $^{239}$Pu of $\sim$ 400 $\mu g/cm^2$ was used. The isomers in the region around $^{132}$Sn are characterize by low-energy isomeric transitions, hence good efficiency and low threshold for the electron-detection are essential. This was achieved by stopping the fragment in a thin (12 $\mu$m) Mylar foil, behind which a cooled Si(Li) detector segmented into two parts and covering an area of $2\times6$ cm$^2$ was placed. The $\gamma$-rays were detected by two large-volume Ge detectors placed perpendicular to the beam. The fission fragments were detected in an ionization chamber of 13.0 cm length and 5.6 cm thickness, built to mount the silicon detectors at the end. The pressure of the gas (isobutane) was tuned to stop the fragment in the Mylar foil at the end of the ionization chamber, in order to minimize the electron absorption and the energy spread.

Set-up 2 was used for an experiment devoted to the even masses. Only the $\gamma$-rays were measured, despite the importance of conversion-electron measurements, but a better resolution in the mass determination was achieved thanks to the two stages of the ionization chamber. The total length of the gas chamber was 15.3 cm, divided into $\Delta E_1$=9.4 cm and $\Delta E_2$=5.8 cm, and its thickness was 6.0 cm. At the end of the second stage 6 pin-diodes were placed to improve the charge resolution for light fragments, but they were not used in the present experiment. The In isotopes measured in the even-mass chains $A = 126, 128, 130$ were already known to have an isomeric transition leading directly to the ground state, whose lifetimes were either unknown or known with big uncertainties. The main purpose of this experiment was the measurement of these lifetimes, along with the search for new isomers in the cadmium isotope members of the selected mass chain, therefore the most important goals to achieve were good $A$ resolution and high efficiency for $\gamma$-ray detection. Consequently, an ionization chamber with a better resolution, but without the possibility of mounting the Si detector, was used. An example

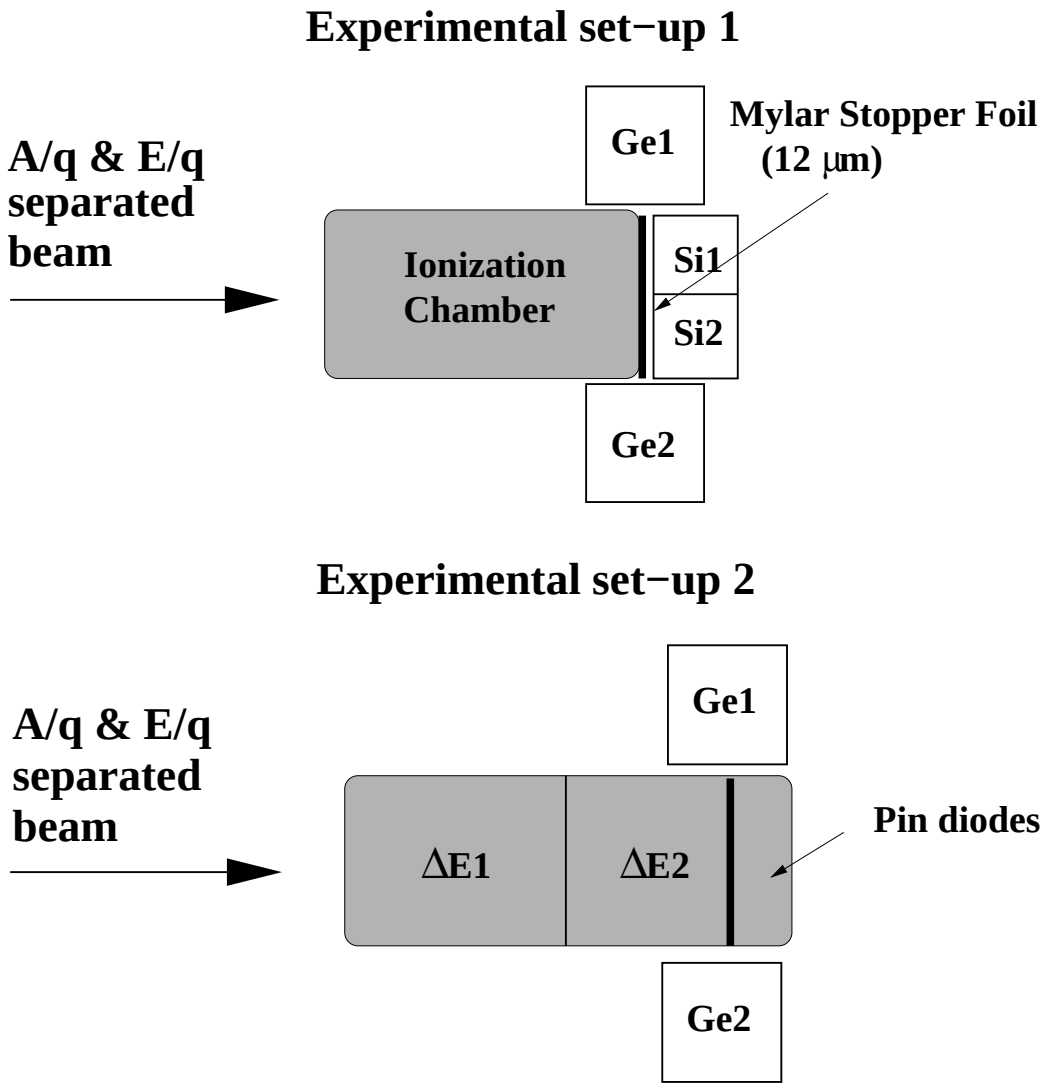


Figure 2.5: Schematic representation of the two experimental set-ups used to measure In and Cd isotopes. Experimental set-up 1: Ge1 and Ge2 are two 60 % HP germanium detectors, Si1 and Si2 are two adjacent cooled Si(Li) detector covering a total area of $2 \times 6$ cm$^2$. Experimental set-up 2: Ge1 is a Clover detector, Ge2 is a Miniball detector and $\Delta E1$, $\Delta E2$ are the fragment energies measured in the two stages of the ionization chamber.

of a spectrum of the ionization chamber is shown in fig. 2.6.

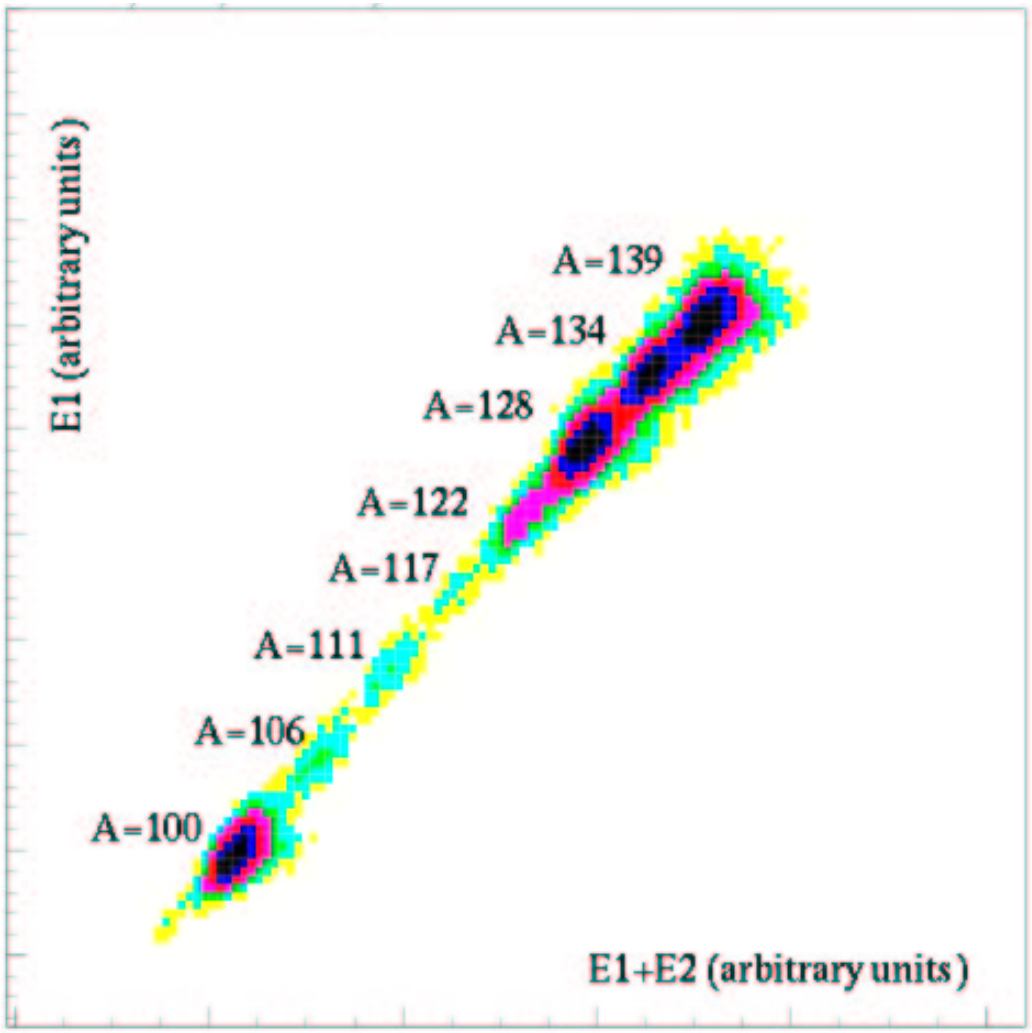


Figure 2.6: $E_{tot} = \Delta E1 + \Delta E2$ versus $\Delta E_1$. LOHENGRIN was optimized for mass $A = 128$.

The $\gamma$-rays were detected by a Clover detector and a Miniball detector, with much higher efficiency compared with set-up 1. In both the cases, the detectors were packed in very close configurations, thanks to the small size of the two ionization chambers used, to achieve high efficiency even with a small number of detectors.

### 2.3.1 The Clover detector

The Clover detector [35] has been developed by a French/U.K. collaboration for the Euroball spectrometer. It consists of four coaxial n-type Ge detectors, arranged like a four-leaf clover (see fig. 2.7). Each detector has a square front face with round edges, in order to enable a close packing of the detectors in the front - the Ge-Ge distance is about 0.2mm - and retaining most (89%) of the original crystal volume. The four detectors are mounted in a common cryostat of tapered rectangular shape.

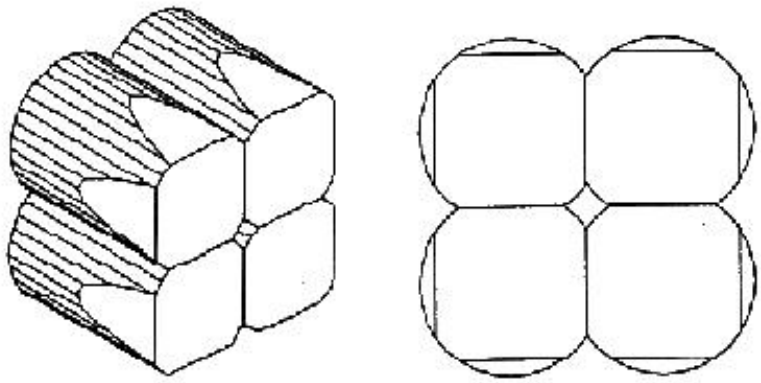

Figure 2.7: The Clover detector.

### 2.3.2 The Miniball detector

The Miniball triple cluster [36] used here is the result of a German/Belgian collaboration which envisaged the construction of a detector type suited for the use with low intensity exotic beams. Since the exotic beams are frequently used in reactions with inverse kinematics, these detectors needed high granularity to correct for Doppler broadening, in addition to high efficiency. This was achieved by a six-fold segmentation of the outer contacts. For the experiment described here, however, only the high efficiency was needed, and it was provided by the three encapsulated crystals closely packed together as shown in fig. 2.8.

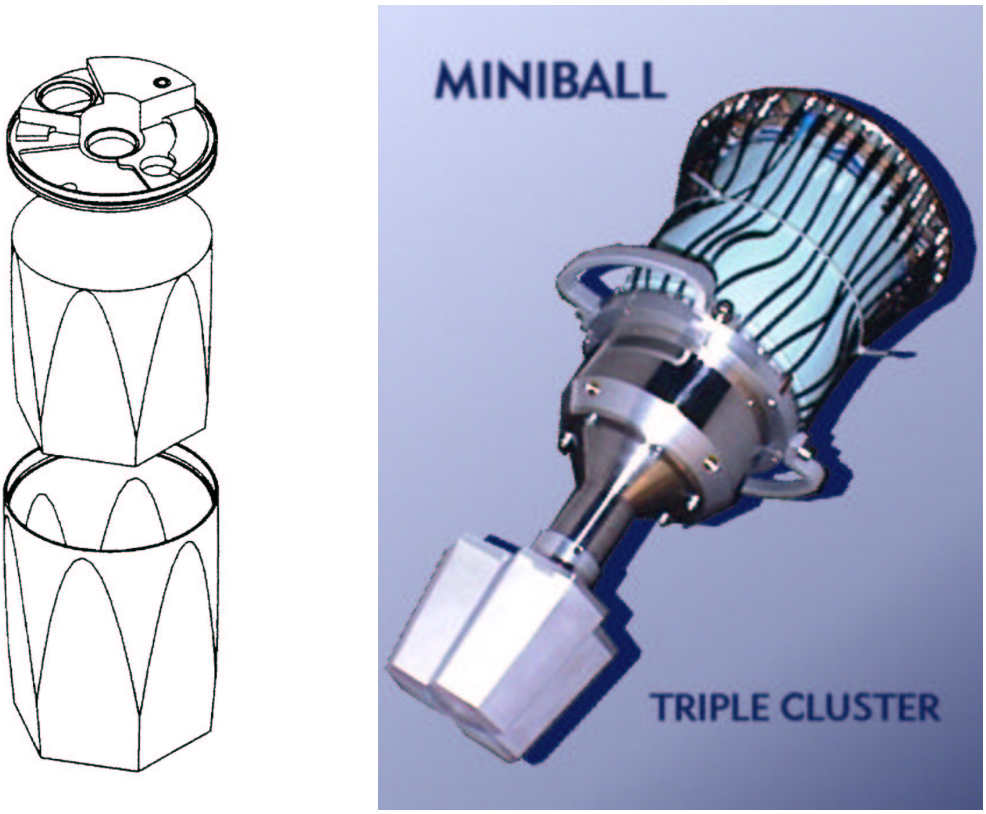


Figure 2.8: The Miniball detector.

## 2.4 Acquisition system and data analysis

Every time a fragment was detected in the ionization chamber (START), all the signals coming from the chamber, the germanium and the silicon detectors were stored on a disk within a 40 $\mu$s time-window (STOP). The time-stamps of the signals originating from a 40 Mhz clock were also recorded, therefore it was possible to build the $\gamma$-$\gamma$, $\gamma$-electron and electron-electron matrices. The single spectra were also collected, to identify new isomeric decays by subtracting the spectrum of the events recorded at the end of the 40 $\mu$s window (region 2 in fig. 2.9) from the spectrum of the events recorded in the first part of the 40 $\mu$s window (region 1 in fig. 2.9).

An example of the power of this technique is shown in fig. 2.9 and 2.10,

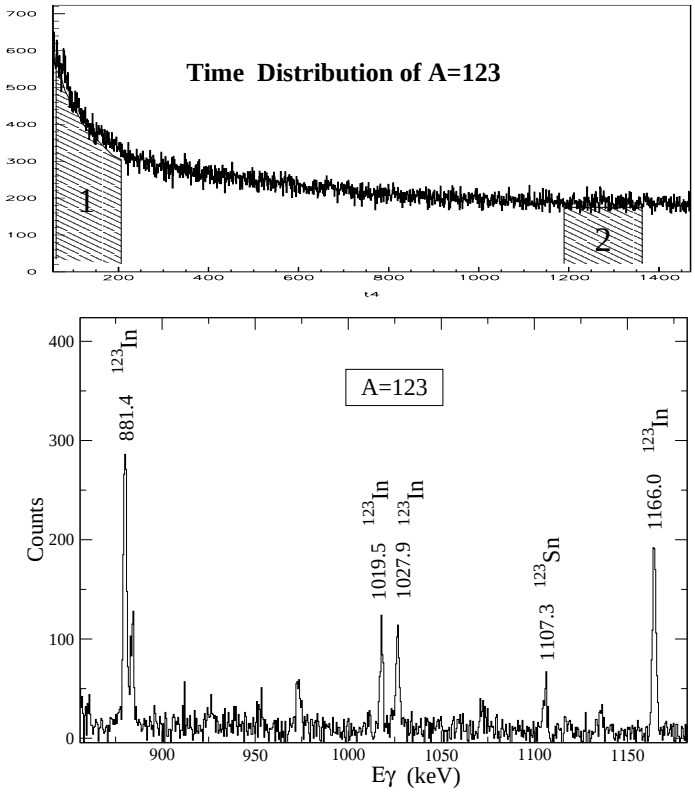


Figure 2.9: Top part: Time distribution of mass $A = 123$. Bottom part: Germanium spectra obtained subtracting, after normalization, the spectrum in coincidence with region 2 from the spectrum in coincidence with region 1. Only the peaks belonging to $^{123}$In and $^{123}$Sn are labelled.

and explained in the following. The time distribution of mass $A = 123$ in fig. 2.9 is simply the time spectrum of the germanium detectors obtained in coincidence with mass $A = 123$. The germanium spectrum corresponding to the whole time distribution in shown in fig. 2.10. The isomeric cascades of $^{123}$In and $^{123}$Sn, whose $\gamma$-rays are labelled, are just visible. The other peaks correspond to other -unfortunately already known- isomers, or $\beta$-decay background. The two germanium spectra obtained in coincidence with region 1, where the isomeric cascades are present, and region 2, considered as background due to random events, can be subtracted after normalization, and the result is shown in fig. 2.9. The isomeric decay-cascades are eventually well

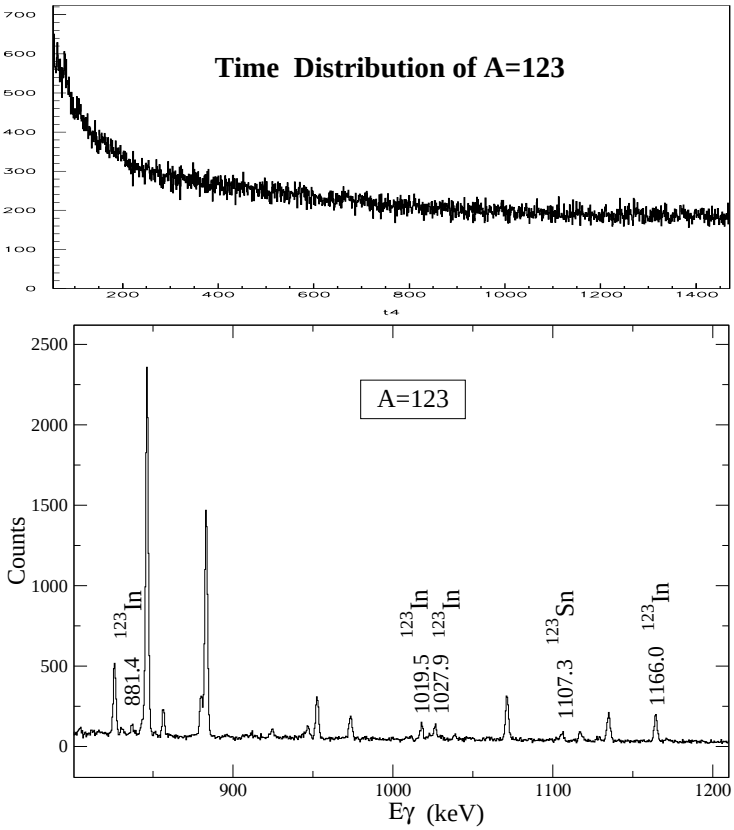


Figure 2.10: Top part: time distribution of mass $A = 123$. Bottom part: Germanium spectrum of the mass $A = 123$ corresponding to the whole time distribution.

enhanced. This is the process which leads to the spectra called in the following: *spectra in delayed coincidence with fission fragments*. The level-schemes of the nuclei under study have been built considering $\gamma-\gamma$, $\gamma-e^-$ and $e^--e^-$ coincidences, and the intensity relationship between the observed transitions. In the case of an isomer, all the intensity is in the isomeric transition, therefore the intensity balance greatly helps in building the level schemes. The multipolarities of the converted transitions were deduced from the conversion coefficients, as explained in chapter 1. The knowledge of the multipolarities allows spins and parities of the levels below the isomers to be deduced.

### 2.4.1 Efficiency

The intensities of $\gamma$-rays have to be corrected to account for the different efficiency of the detectors at different energies.

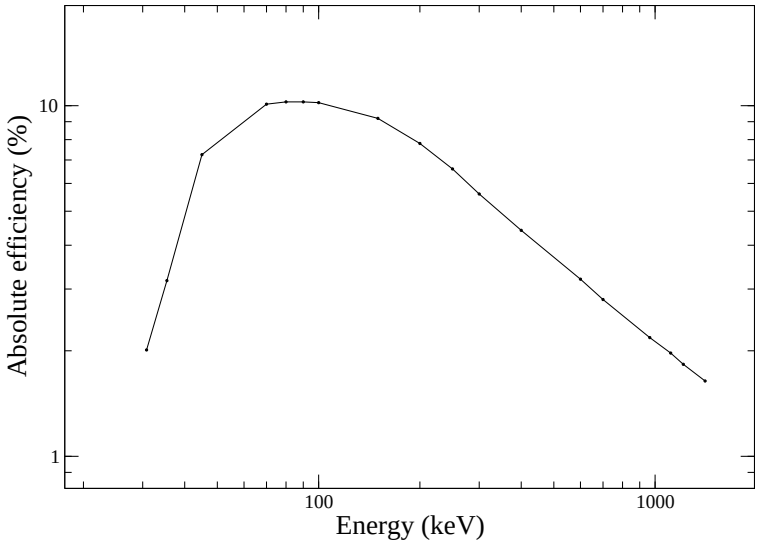


Figure 2.11: Absolute efficiency of the Clover detector.

The relative efficiencies were deduced from the $\beta$-decay peaks present in the single spectra. In some favorable cases, as for example $^{136}$Xe, $^{94}$Y, $^{95}$Y, $^{88}$Br etc.., there are isomeric cascades in strongly produced isotopes without crossover transitions. Due to the high intensity, the summed energy in the detectors of two of the transitions of the cascade can be observed. The probability $P$ of this event is:

$$P = \epsilon_1 \cdot \epsilon_2, \tag{2.18}$$

where $\epsilon_1$ and $\epsilon_2$ are the absolute efficiencies for the detection of the two transitions respectively. The area of the peak due to the pile-up $I = NP$, being $N$ the number of nuclei, can be written as:

$$I = NP = N\epsilon_1\epsilon_2 = I_{\gamma_1}\epsilon_2 = I_{\gamma_2}\epsilon_1, \tag{2.19}$$

where $I_{\gamma_1}$ and $I_{\gamma_2}$ are the areas of the peak $\gamma_1$ and $\gamma_2$ respectively. The two ratios $I/I_{\gamma_1}$ and $I/I_{\gamma_2}$ give the absolute efficiency of the detectors at

the energy $\gamma_2$ and $\gamma_1$ respectively. An example of absolute-efficiency curve obtained with this method is shown in fig. 2.11 for the Clover detector. With the set-up 2 the total efficiency at 100 keV was 20%, at 30 keV 1.9% and at 1 MeV 4%.

# Chapter 3

# Experimental Results

Three experiments were carried out at the LOHENGRIN separator to extend the scarce experimental information on the In and Cd isotopes with $A \geq 123$. The aim of the first two experiments was to search for $\mu$s isomers in the odd-masses, using $^{239}$Pu and $^{241}$Pu as targets. The third experiment was devoted to the even-masses and a target of $^{241}$Pu was used. In this chapter the experimental results obtained are reported.

## 3.1 $^{123}$In

A new $\mu$s isomer has been discovered in $^{123}$In. In the $\gamma$-decay spectrum of the mass $A = 123$ in delayed coincidence with the fission fragments, shown in fig. 3.1, four unassigned $\gamma$-lines (880.7, 1019.0, 1027.4 and 1166.0 keV) are present. Two $\gamma$-rays of 1027.5 and 1165.9 keV respectively, have been observed in $\beta$-decay studies of $^{123}$Cd to $^{123}$In [4]. They de-excite two levels of $^{123}$In with possible spin and parity assignments of $11/2^+$ and $13/2^+$ respectively. The fact that we observe two transitions with almost the same energy, and the absence of any common $\gamma$-rays belonging to the known isomer of $^{123}$Sn [37], the only element along with $^{123}$In which has sufficient production yield, allow this isomer to be attributed to $^{123}$In. The $\gamma$-ray of $\sim$ 138 keV connecting the $13/2^+$ level to the $11/2^+$ level (see level-scheme in fig. 3.10) was not observed, due to the low expected relative intensity ($\sim 7$) deduced from the intensities of the observed transitions reported in table 3.1.
The half-life of the isomer is 1.4(2) $\mu$s, as shown in fig. 3.1 and reported in table 3.4. The $\gamma - \gamma$ coincidences are shown in fig. 3.2.

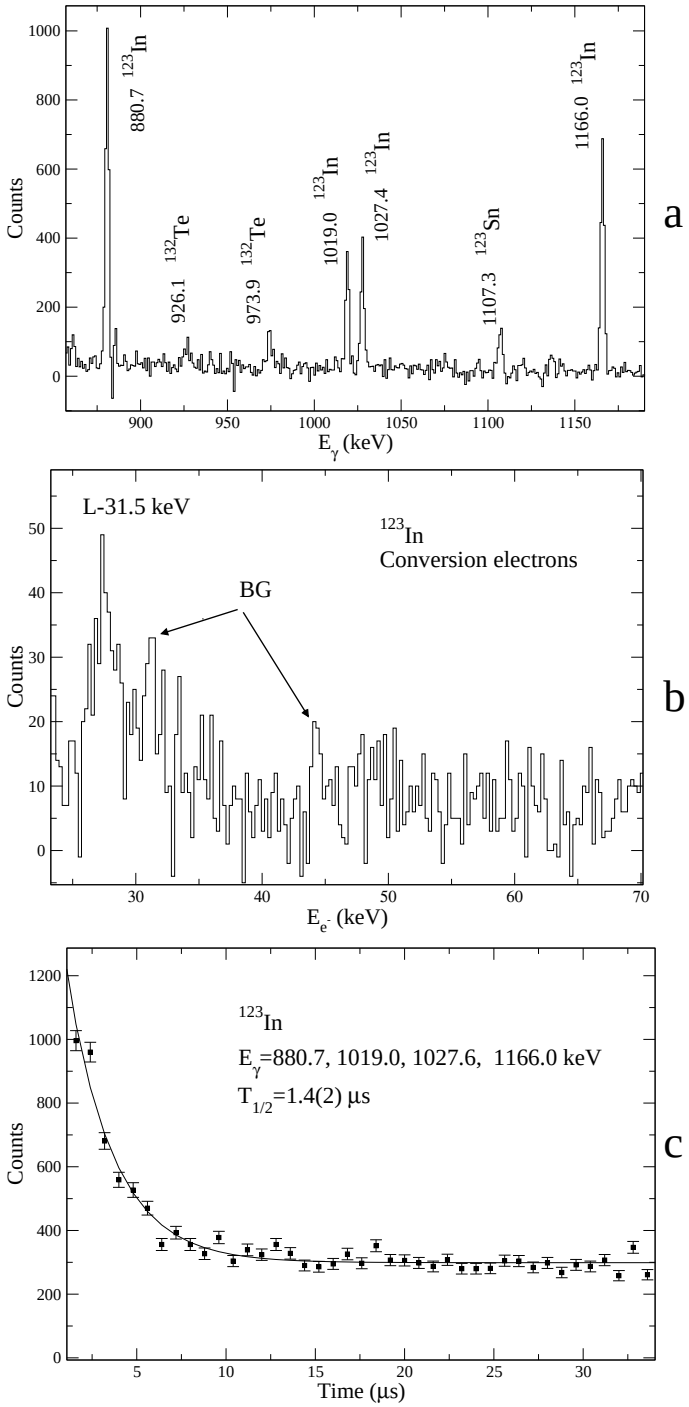


Figure 3.1: a) $\gamma$-decay spectrum of the mass $A$=123 in delayed coincidence with the fission fragments. b) Si(Li) spectrum of the mass $A$=123 in delayed coincidence with the fission fragments. The value 31.5 keV labelled is the energy of the isomeric transition. c) Time spectrum of 880.7, 1019.0, 1027.4 and 1166.0 keV.

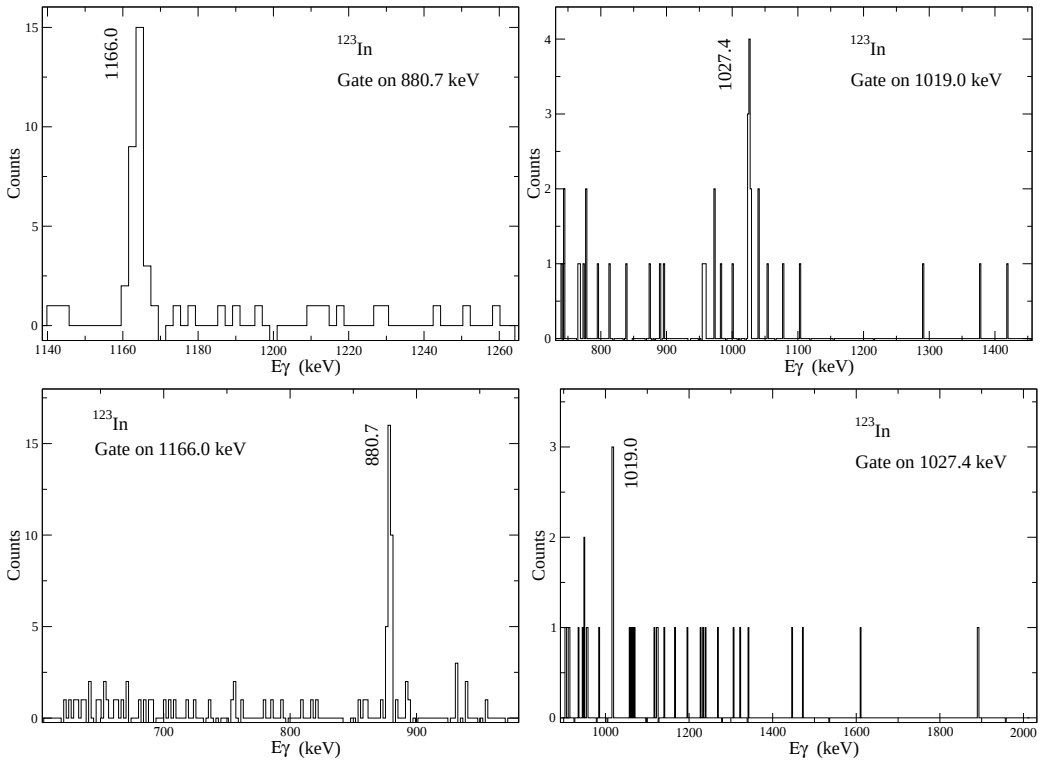


Figure 3.2: $\gamma - \gamma$ coincidences between the four transitions of the isomeric cascade observed in $^{123}$In.

Due to the poor statistics, it was not possible to observe the conversion electrons in coincidence with the $\gamma$-rays of the isomeric decay. However, in

Table 3.1: Relative intensities of the transitions observed in $^{123}$In

| Transition | Transition's energy | Intensity |
|---|---|---|
| $(13/2^-) \rightarrow 13/2^+$ | 880.7(2) | 107 |
| $(13/2^-) \rightarrow 11/2^+$ | 1019.0(3) | 40 |
| $11/2^+ \rightarrow 9/2^+$ | 1027.4(3) | 42 |
| $13/2^+ \rightarrow 9/2^+$ | 1166.0(3) | 100 |

the Si(Li) spectrum in delayed coincidence with the fission fragments of mass $A$=123, an electron line of 27.5(5) keV, decaying with a half-life comparable to the $\gamma$ cascade was observed (see fig. 3.1b). The non-observation of another electron group suggests that this line corresponds to L conversion electrons from a transition of 31.5(5) keV. A value so close to the binding energy of the K electrons explains the non-observation of the K-X rays. Assuming that this low-energy transition has an $E2$ multipolarity, as suggested by the absence of cross-over transition between the 2078.5 keV level and the 1165.8 keV level and by analogy with the neighboring nuclei, a value of $B(E2)$=3.3(5) W.u. can be deduced.

## 3.2 $^{127}$In

A 9(2) $\mu$s isomer which decays by a cascade consisting of a strongly-converted $E2$ transition of 47.0(5) keV, followed by $\gamma$-rays of 221.3(5) and 233.4(5) keV in coincidence with one another (fig. 3.3) has been observed. The two $\gamma$-rays are the same as those first observed by Hellström *et al.* [8], and the reported value of the half-life, 13(2) $\mu$s, is in rough agreement with the one found in this work, as reported in table 3.4. These authors have also reported an abnormally high number of counts in the first 500 ns interval of the time spectrum, and suggested the possible presence of two isomeric states. We have not observed the short component in our data and we feel that, if it exists, its half-life is shorter than $\sim$0.5 $\mu$s, the LOHENGRIN detection limit. The Si(Li) spectrum obtained in coincidence with any of these two lines (fig. 3.3b) shows the characteristic indium X-rays, and the K and L conversion electrons of the isomeric transition of 47 keV.

Table 3.2: Calculated K over L ratios for a transition of 47 keV in $^{127}$In

| Transition's multipolarity | K/L ratio |
|---|---|
| E1 | 6.1 |
| M1 | 6.5 |
| E2 | 0.9 |

The large broadening of the K-electron line, due to absorption in the Mylar foil of the low energy electrons (19 keV), does not allow a precise

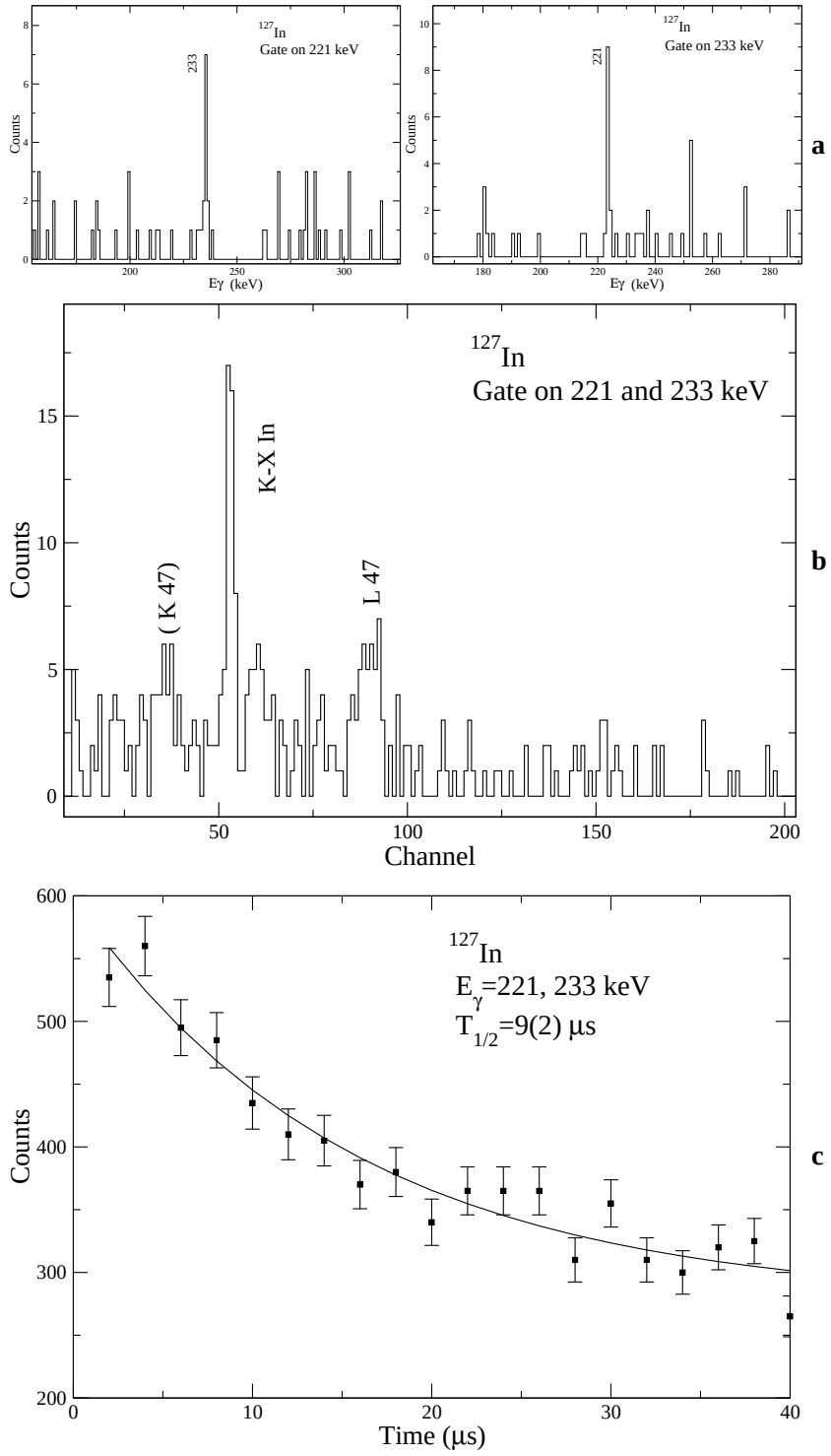


Figure 3.3: a) Coincidence spectra gated on the $\gamma$-ray of 233 or 221 keV. b) Si(Li) spectrum obtained in coincidence with the $\gamma$-rays of 221 and 233 keV. c) Time spectrum of 221 and 233 keV $\gamma$-rays.

evaluation of the peak's area. Consequently, the X-rays over L-electrons ratio was used to deduce the multipolarity. The comparison between the experimental finding X/L=1.2(3), and the calculated values in table 3.2, suggests an $E2$ multipolarity. A $B(E2)$=0.30(7) W.u. value can be obtained.

## 3.3 $^{129}$In

Four $\gamma$-rays of 333.8, 359.0, 995.2, 1354.1 keV respectively have been found corresponding to the decay of an isomer of 8.5(5) $\mu$s. The relative intensities of these lines are reported in table 3.3.

Table 3.3: Relative intensities of the transitions observed in $^{129}$In

| Transition | Transition's energy | Intensity |
|---|---|---|
| $17/2^- \rightarrow 13/2^+$ | 333.8(2) | 100 |
| $13/2^+ \rightarrow 11/2^+$ | 359.0(2) | 83 |
| $11/2^+ \rightarrow 9/2^+$ | 995.2(3) | 82 |
| $13/2^+ \rightarrow 9/2^+$ | 1354.1(4) | 28 |

Figure 3.4a shows the $\gamma$ spectrum of the mass chain $A = 129$ in delayed coincidence with the fission fragments, where, along with the known isomer of $^{129}$Sn [38], the new cascade is also present. Figure 3.4b shows the time spectrum obtained in coincidence with the transition of 333.8 keV. The half-life given in the text and reported in table 3.4 is the result of an average of the values measured for the four lines of the cascade de-exciting the isomer. The presence of the characteristic indium X-rays and the K and L conversion electrons of the 333.8 keV transition in coincidence with the three other transitions of the cascade (fig. 3.4b) allow the attribution of this isomer to $^{129}$In, and the evaluation of the conversion coefficient. Its value $\alpha_k = 0.08(2)$ is compatible either with an $M2$ ($\alpha_k = 0.071$) or with an $E3$ ($\alpha_k = 0.063$) multipolarity. The transition probabilities obtained assuming pure $M2$ or $E3$ multipolarities are $B(M2) = 0.032(2)$ W.u. and $B(E3) = 279(16)$ W.u respectively, hence, as accelerated $E3$ transitions are not expected, one may conclude that the transition has predominantly an $M2$ character.
The $\gamma - \gamma$ coincidences between the four transitions of the cascade are reported in fig. 3.5.

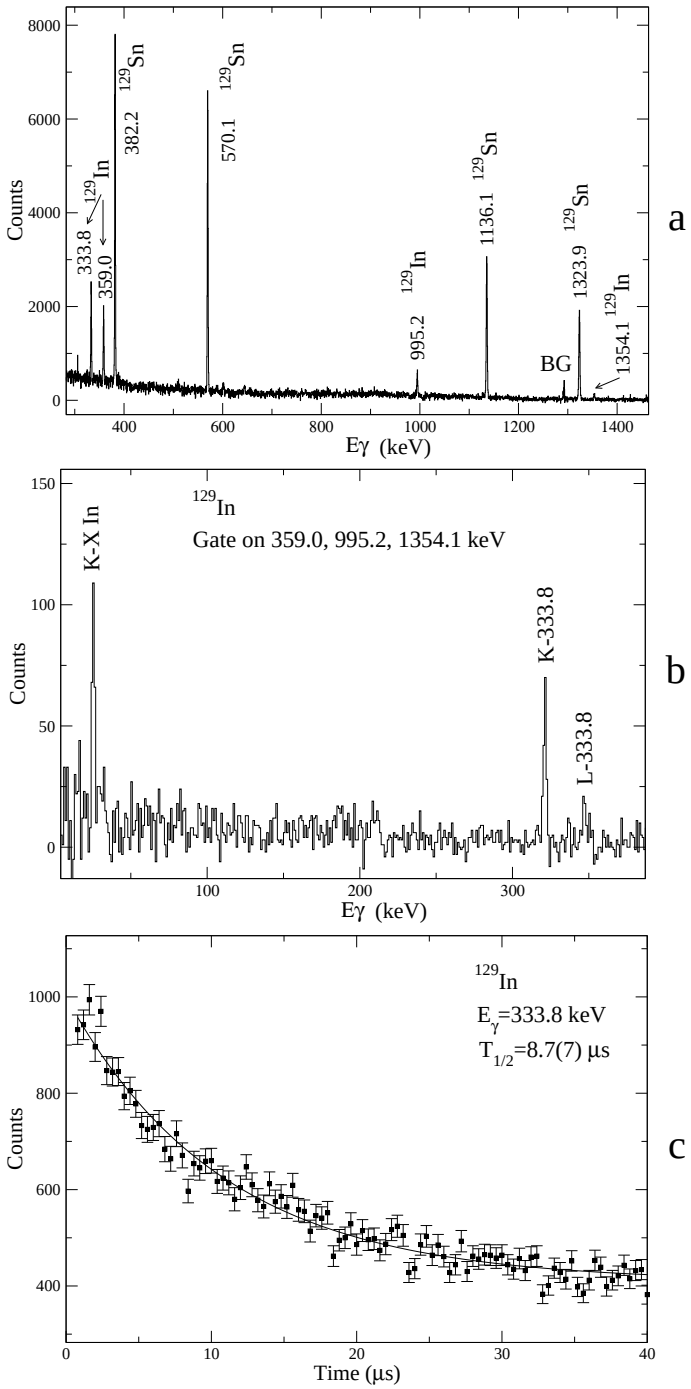


Figure 3.4: a) $\gamma$-ray spectrum of the mass $A = 129$ in delayed coincidence with the fission fragments. b) Si(Li) spectrum obtained in coincidence with the $\gamma$-rays of 359.0, 995.2 and 1354.1 keV. c) Time spectrum of 333.8 keV.

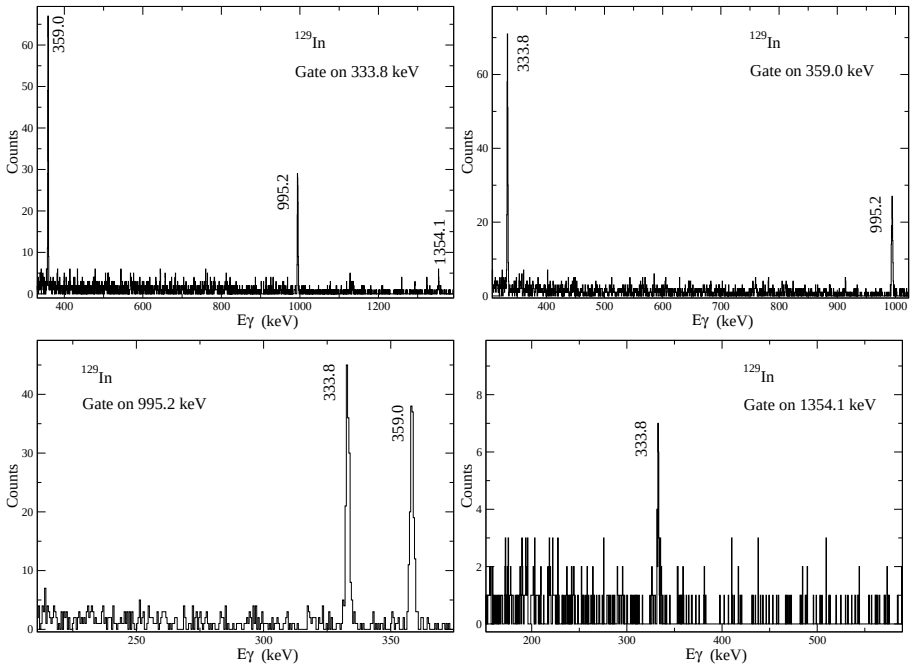


Figure 3.5: $\gamma - \gamma$ coincidences between the four transitions of the isomeric cascade observed in $^{129}$In.

## 3.4 Odd-odd Indium isotopes

In the even-mass $^{130}$In, $^{128}$In, and $^{126}$In the presence of an isomeric transition (388.8, 247.9 and 243.2 keV respectively) feeding directly the ground state is known (see ref. [8, 9, 39]). The half-life of these transition, in particular in the case of $^{130}$In and $^{128}$In, is either unknown, or known with big uncertainty (see table 3.4).

In this work, the half-lives of these three transitions were measured [32], and the results are reported in table 3.4 along with the values obtained in previous works [8, 9]. As mentioned before, in the case of $^{128}$In the value measured in this work is in agreement with the previous one, but is much more precise, whereas in the case of $^{126}$In the two result are not equal within the experimental errors. For $^{130}$In no measured value was available, but only an indication of the range before this work. The time spectra of the three In isotopes investigated are shown in fig. 3.6. The spins and parities reported in table 3.4 for $^{126}$In are assigned by analogy with the neighboring

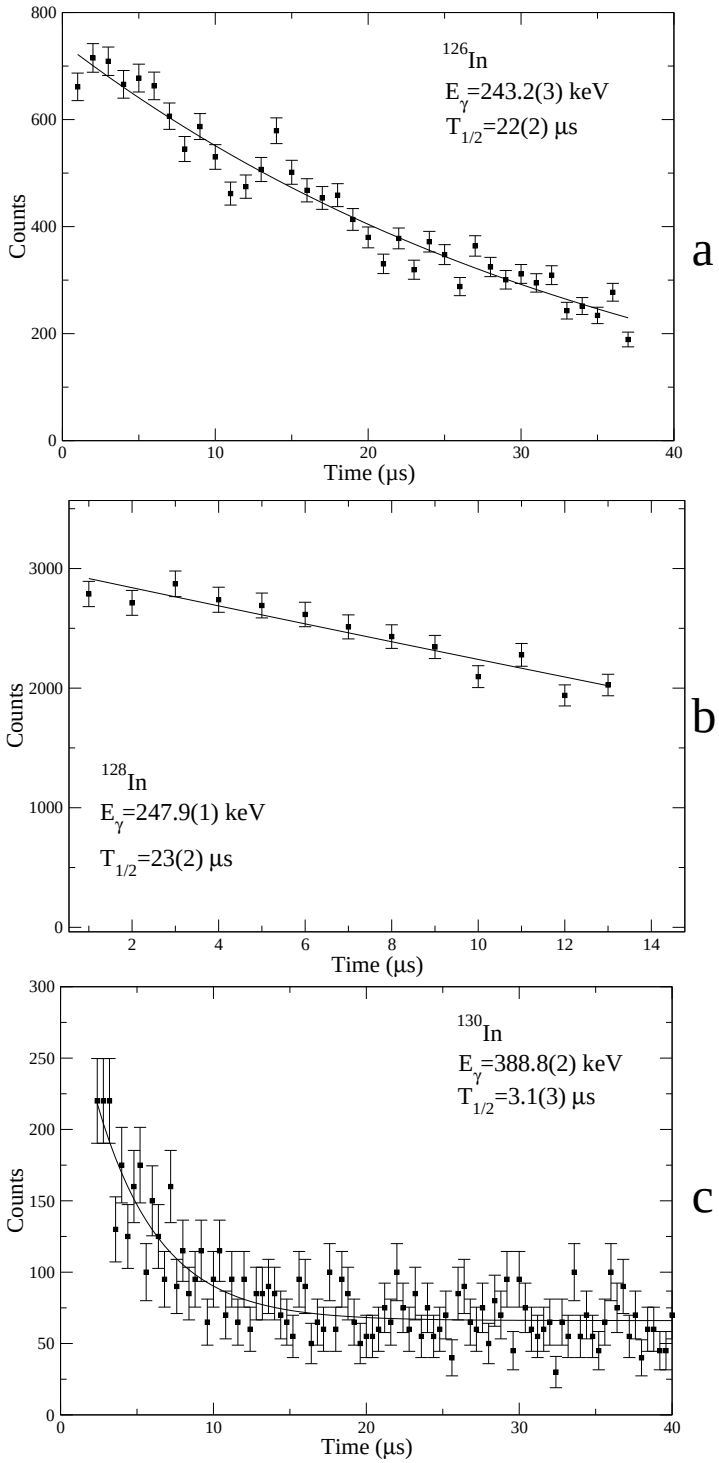


Figure 3.6: Time spectrum of $^{126,128,130}$In.

$^{128}$In. However, it cannot be completely excluded that the 243.2 keV $\gamma$-ray connects a higher-lying isomeric state with the $8^-$ $\beta$-decaying level.

## 3.5 Cadmium isotopes

Two $\mu$s isomers have been reported by Hellström *et al.* [9] in the odd-mass $^{127}$Cd and $^{125}$Cd respectively. The two $\gamma$ lines of 720 and 743 keV belonging to $^{125}$Cd were observed in the $\gamma$ spectrum of mass $A = 125$ in delayed coincidence with the fission fragments shown in fig. 3.8a, but not the $\gamma$-ray of 820 keV assigned to $^{127}$Cd.

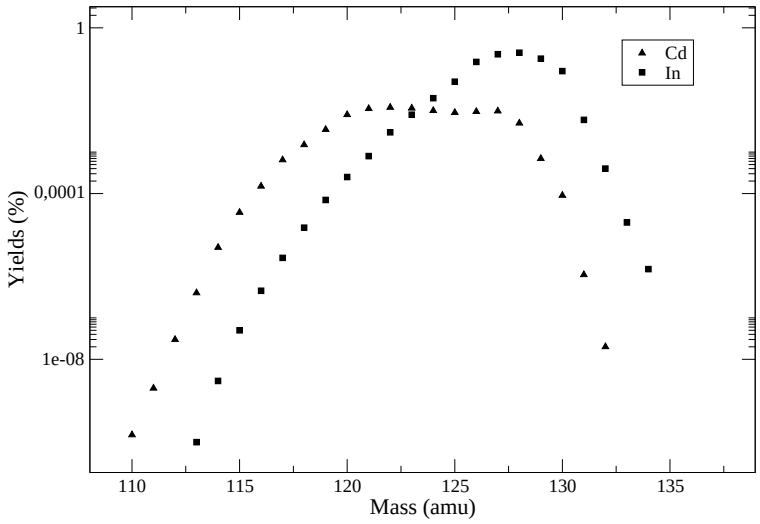


Figure 3.7: Predicted fission yields for In and Cd isotopes provided by Prof. Rubchenya.

Furthermore, both in this work and the work quoted above was found no evidence of $\mu$s isomerism in the even-mass Cd isotopes. If $^{130}$Cd, with the predicted fission yield lower than $10^{-6}$, is perhaps not experimentally observable, $^{126,128}$Cd, with fission yields of the order of $10^{-4}$, the same as the above mentioned $^{125}$Cd, should be observed. This fact most likely means that the existence of isomers with half-lives longer than 0.5 $\mu$s can be excluded. The fission yields have been provided by Prof. Rubchenya using the method described in Chapter 2 and [24]. The results are shown in fig. 3.7.

### 3.5.1 $^{125}$Cd

The isomer of $^{125}$Cd decays by two $\gamma$-lines of the same intensity of 719 and 743 keV respectively (see fig. 3.9 and 3.8). The half-life of the cascade is 19(2) $\mu$s. In fig. 3.8 the time spectrum and the germanium spectrum in delayed coincidence with the fission fragments are shown.

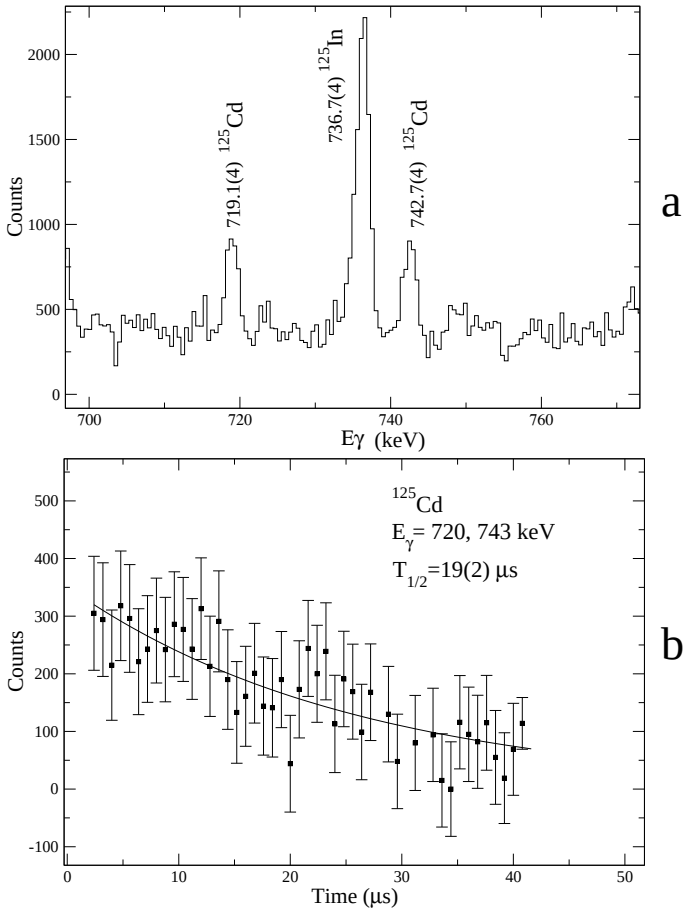


Figure 3.8: a) Germanium spectrum obtained in delayed coincidence with mass $A = 125$. b) Time spectrum of $^{125}$Cd.

No conversion electrons were observed in coincidence with any of the two $\gamma$-rays, but the low statistics does not allow a firm conclusion on this point and leaves the door open for further investigation. The only experimental

information on this nucleus is the presence of an $11/2^-$ $\beta$-decaying isomer at about 50 keV above the $3/2^+$ ground state [40]. The spins and parity assignments of these two levels and their relative energy are not firmly established. The cascade observed in this work most likely end at the $11/2^-$ state.

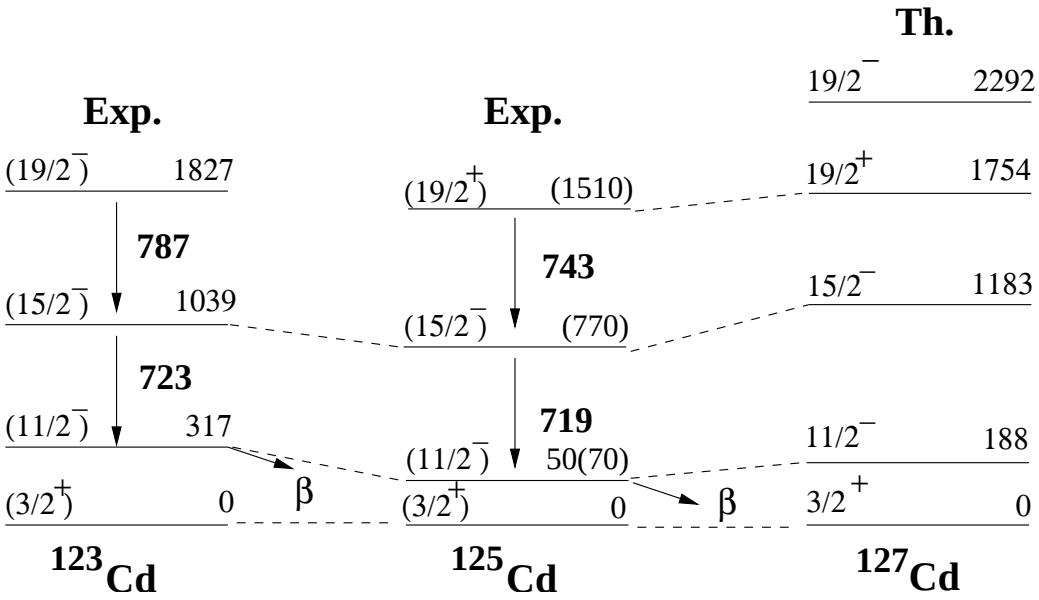


Figure 3.9: Experimental levels of $^{125}$Cd in comparison with experimental levels of $^{123}$Cd and a theoretical calculation on $^{127}$Cd. The energies are given in keV.

A tentative level scheme is proposed in fig. 3.9, where $^{125}$Cd is compared with its neighbor $^{123}$Cd and a shell-model calculation on $^{127}$Cd. A description of the theoretical shell-model calculations performed in this work is given in chapter 4. The order of the transitions in fig. 3.9 is arbitrary and could be inverted. Assuming pure $M2$ or $E3$ multipolarities, $B(M2) = 4.5\times10^{-5}$ W.u. or $B(E3) = 0.7$ W.u. can be deduced.

## 3.6 Level schemes of odd-In nuclei

The heavy In and Cd nuclei, with neutron and proton holes inside the $^{132}$Sn core, are characterized by the presence of two high-spin states, $\pi g_{9/2}^{-1}$ and $\nu h_{11/2}^{-1}$, at low excitation energy.

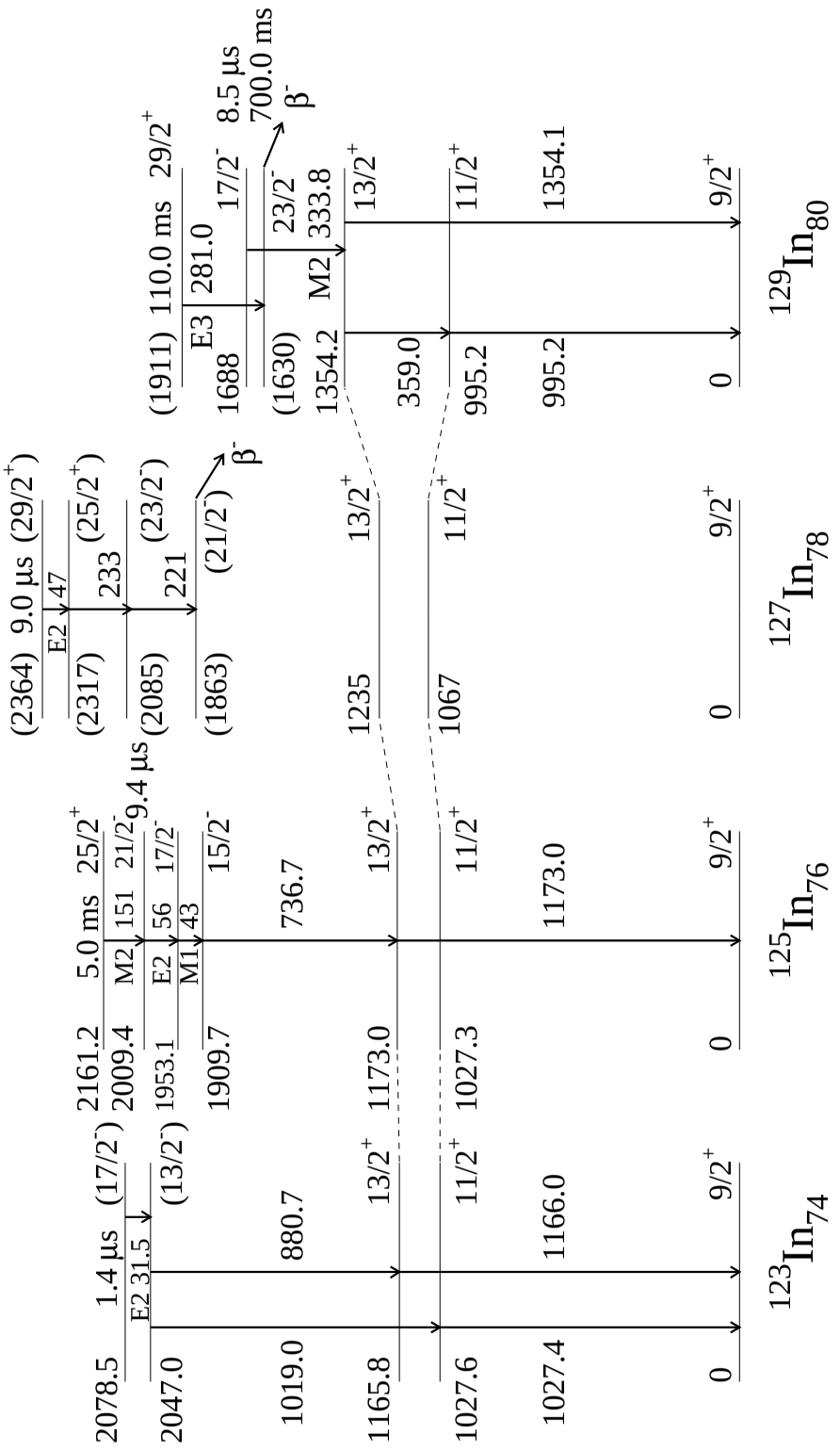


Figure 3.10: Level schemes of $^{123,125,127,129}$In. The level energies (keV) in parenthesis are deduced from $\beta$ spectra [6] and have large uncertainties.

The $p-n$ interaction in the $(\pi g_{9/2}^{-1}\nu h_{11/2}^{-1})_{10^-}$ state is very strong and is expected to produce very perturbed yrast lines. These features greatly complicate the construction of the level schemes and therefore different experimental techniques are needed to study these nuclei. The level schemes of $^{123-129}$In shown in fig. 3.10 are the result of the synthesis of different works: the ms isomer experiments performed at the OSIRIS mass separator [6, 7], and the $\mu$s isomer experiments performed with the LOHENGRIN spectrometer [32, 33]. All the reported levels are in the vicinity of the yrast line, therefore the low-spin levels fed by $\beta$-decay are not shown in fig. 3.10.

### 3.6.1 $^{129}$In

In $^{129}$In, ms and $\mu$s isomers are present. Fogelberg *et al.* [7] have shown evidence of a high-spin $29/2^+$ yrast trap which decays by an $E3$ transition (110 ms half-life) to another yrast trap of spin $23/2^-$ (half-life 700 ms), which $\beta$ decays to $^{129}$Sn. Recently a more precise value of the excitation energy, 1630(56) keV, was measured for the $23/2^-$ state in $\beta$-decay experiments [6]. Beyond this transition, only the ground state $9/2^+$ was known, therefore the isomeric cascade studied in this work constitues the first substantial spectroscopic information on this nucleus. The spin and parity assigments of fig. 3.10 are deduced from the $M2$ multipolarity of the isomeric transition on the top of the cascade, the relative intensities of the transitions in table 3.3 and the $\gamma$-$\gamma$ coincidences.

### 3.6.2 $^{127}$In

The isomeric cascade observed in this isotope has no overlap with the previously known $\gamma$-rays which feed directly or indirectly the $1/2^-$ isomer of 420(65) keV energy [5, 6]. Moreover, the comparison with the neighboring $^{125}$In and $^{129}$In shows that the excited states above the $9/2^+$ ground state have energies higher than $\sim$1 MeV, which excludes the possibility that the observed cascade ends at this level. Consequently, this cascade most likely de-excites a $29/2^+$ isomer to a $21/2^-$ state, decaying itself by $\beta$ emission. This finding agrees with the measurement of Gausemel *et al.* [6] who have found a $21/2^-$ isomer in $^{127}$In of 1.0 s half-life and have deduced its energy to be 1863(58) keV, from $\beta$-decay spectra. In figure 3.10 the order of the transitions of 221 and 233 keV respectively is arbitrary and could be inverted. Two other states at energies of 1067 keV and 1235 keV, feeding directly the

Table 3.4: Half-lives measured in the present work along with the already known values.

| Nucleus | Transition | half-life ($\mu$s) This work [32, 33] | half-life ($\mu$s) Previous work [8, 9] |
|---|---|---|---|
| $^{123}$In | $17/2^- \rightarrow 13/2^-$ | 1.4(2) | - |
| $^{127}$In | $29/2^+ \rightarrow 25/2^+$ | 9(2) | $< 0.5$ and 13(2) |
| $^{129}$In | $17/2^- \rightarrow 13/2^+$ | 8.5(5) | - |
| $^{126}$In | $1^- \rightarrow 3^+$ | 22(2) | 29(2) |
| $^{128}$In | $1^- \rightarrow 3^+$ | 23(2) | 175(90) |
| $^{130}$In | $3^+ \rightarrow 1^-$ | 3.1(3) | 1-10 |
| $^{125}$Cd | $19/2^+ \rightarrow 15/2^-$ | 19(2) | 14(2) |

$9/2^+$ ground state are added to the level scheme. They were reported by Hoff *et al.* [5] but without spin and parity assignments. By analogy with $^{125}$In and $^{129}$In, spin and parity assignments of $11/2^+$ and $13/2^+$, respectively, are proposed.

### 3.6.3 $^{125}$In

Fogelberg *et al.* [7] have found a 5 ms isomer in $^{125}$In which decays by an $M2$ transition to a 9.4 $\mu$s isomer which itself decays by a $\gamma$-ray cascade to the $9/2^+$ $^{125}$In ground state. The decay of the $\mu$s isomer have been observed in this work, in agreement with the proposed level scheme and the $E2$ and $M1$ mutipolarities measured for the 56 and 43 keV transitions respectively. Fogelberg *et al.* have suggested a spin and parity assignment of $23/2^-$ for the ms isomer, and positive parities for the states below the isomer. However, this hypothesis seems inconsistent with the non-observation, confirmed by the present measurements, of the cross over between the 1953.1 keV and 1173.0 keV levels and between the 1909.7 and 1027.3 keV levels respectively. A $25/2^+$ spin and parity assignment for the ms isomer and a change of parity for the three successive levels seem necessary to explain these findings and is reported in fig. 3.10.

### 3.6.4 $^{123}$In

The isomer in $^{123}$In decays by a low energy transition expected to be $E2$ and a $\gamma$-ray cascade to the $9/2^+$ ground state. The simultaneous feeding of the $11/2^+$ and $13/2^+$ levels at 1027.6 and 1165.8 keV, respectively, deduced from the intensities in table 3.1 and the $\gamma$-$\gamma$ coincidences, suggests a spin and parity assignment of $13/2^-$ or $15/2^+$ for the 2047.0 keV level. The negative parity assignment is preferred by analogy with the heavier In isotopes and is reported in fig. 3.10, but a positive parity cannot be completely ruled out.

# Chapter 4

# Shell-model calculations and discussion

In this chapter the shell-model calculations performed for the nuclei under study are described. The comparison between the experimental results presented in chapter 3 and the outcome of the theoretical shell-model calculations described in section 4.1 is discussed. While it would be very interesting to compare experiment and theory for all the nuclei investigated, unfortunately the number of configurations becomes too large to allow calculations for $^{125}$In and $^{123}$In with the OXBASH code [41].

## 4.1 Shell model calculations

A basic input for nuclear shell-model calculations is the effective interaction $H_{eff}$. In the past several empirical interactions have been constructed, some of them very successful in describing a large number of nuclei, but it was the advent of realistic $NN$ potentials that has created a challenge for nuclear structure theory: the description of nuclei with a high number of nucleons starting from free $NN$ interactions. Pioneering works in this direction were performed by Kuo and Brown [42], Kuo and Herling [43], both based on the Hamada-Johnston potential [44]. The results were used in extensive calculations focussed on the region around the doubly magic $^{208}$Pb [45]. More recently, new high-quality $NN$ potentials have been constructed, using as an experimental constraint the 1992 Nijmegen database [46] of free neutron-proton ($n-p$) and proton-proton ($p-p$) data, which contains 1787 $p-p$ and

2514 $n-p$ experimental points below 350 MeV. Among these potentials, the CD-Bonn potentials gives the most accurate reproduction of the experimental data [47].

The shell model study of the indium and cadmium isotopes has been performed using a realistic effective interaction derived from the CD-Bonn nucleon-nucleon ($NN$) potential by the group of Prof. Covello at Napoli University in the hole-hole formalism. A description of the method used to derive the matrix elements can be found in [11] and references therein. The effective interaction obtained contains only the two-body terms which represent all the possible interactions between two valence holes in the orbitals included in the chosen configuration space. The one-body terms, e.g. the single particle energies, were deduced from the experimental spectrum of $^{131}$In and $^{131}$Sn [48], except the energy of the $1h_{11/2}$, whose adopted value is slightly lower than the measured one. This choice is discussed in detail in [12]. The values are reported in table 4.1.

Table 4.1: Single particle energies used in the calculation.

| Neutron-hole level | Energy (MeV) | Proton-hole energy | energy (MeV) |
|---|---|---|---|
| $1d_{3/2}$ | 0.000 | $0g_{9/2}$ | 0.000 |
| $0h_{11/2}$ | 0.100 | $1p_{1/2}$ | 0.365 |
| $2s_{1/2}$ | 0.332 | $1p_{3/2}$ | 1.650 |
| $1d_{5/2}$ | 1.655 | $0f_{5/2}$ | 2.750 |
| $0g_{7/2}$ | 2.434 | | |

With regards to the configuration space, the $^{132}$Sn nucleus was considered as a closed core. The proton and neutron holes can therefore occupy the levels $2p_{3/2}$, $1f_{5/2}$, $2p_{1/2}$, $1g_{9/2}$ in the 28-50 shell and the neutron holes the levels $1g_{7/2}$, $2d_{5/2}$, $1h_{11/2}$, $2d_{3/2}$, $3s_{1/2}$ in the 50-82 shell. To calculate the electric transition probabilities, the effective charge of proton and neutron are needed. As a result of a study performed on the N=50 isotones [49], the effective proton charge for $^{129}$In and $^{128}$Cd was found to be $e_\pi$=1.35 $e$. The effective neutron charge $e_\nu$=0.78 $e$ has been used because it reproduces correctly the $B(E2; 10^+ \rightarrow 8^+)$ in $^{130}$Sn [33]. In the absence of other experimental or theoretical information, these values have been adopted for all the nuclei

studied. In the calculation of the magnetic transition the free gyromagnetic factors have been used, since a reasonable change in their values slightly affects the final result and no measured values are available. The theoretical results have been obtained using the OXBASH shell model code [41]. Similar calculations have been successfully performed for several nuclei in the region of $^{132}$Sn [11], with few particles or holes outside or inside the closed core $N = 82$, $Z = 50$.

## 4.2 Indium isotopes

### 4.2.1 $^{129}$In

$^{129}$In ($Z = 49$ and $N = 80$) is characterized by one proton hole in the closed shell $Z = 50$ and two neutron holes in the closed shell $N = 82$. The single particle levels closest to the Fermi level are the $\pi g_{9/2}$, $\nu h_{11/2}$ and $\nu d_{3/2}$ orbitals. They are expected to give rise to the excited states found in this work, in agreement with the shell-model calculations. The positive parity states $11/2^+$ and $29/2^+$ are found to be dominated by a unique configuration, $\pi g_{9/2}^{-1} \nu h_{11/2}^{-2}$, whereas the ground state $9/2^+$ and the $13/2^+$ present a significant configuration mixing. The energies of the yrast states are shown in fig. 4.1.
The two resulting negative parity states $23/2^-$ and $17/2^-$ are rather pure, and members of the $\pi g_{9/2}^{-1} \nu (d_{3/2}^{-1} h_{11/2}^{-1})$ multiplet. In table 4.2 the amplitudes of the main configurations contributing to the wave functions of the levels mentioned are reported.

In fig. 4.2a, the experimental and calculated levels of $^{129}$In and $^{130}$Sn [11, 33] are compared. The comparison between these two nuclei is instructive because the levels of $^{129}$In are expected to result from the coupling of a $\pi g_{9/2}$ hole to the two-neutron hole states in $^{130}$Sn. For $^{129}$In, all the experimental levels, except the $1/2^-$ at 369 keV not observed in this work are shown, while in the spectrum of $^{130}$Sn only some selected yrast levels are included.
The dominant configurations of all these states are also indicated. It should be mentioned, however, that a significant configuration mixing is present in some states. More precisely, only the $7^-$ and $10^+$ state in $^{130}$Sn and the $11/2^+$, $23/2^-$, $17/2^-$, and $29/2^+$ states in $^{129}$In have a weight of the dominant configuration larger than about 85%. The excitation energies in $^{130}$Sn are rather well reproduced by the shell-model calculations. However, it is interesting to

Table 4.2: Amplitudes in % of the main configurations contributing to the wave functions of the $9/2^+$, $11/2^+$, $13/2^+$, $17/2^-$, $23/2^-$ and $29/2^+$ levels of $^{129}$In. Only the amplitudes bigger than 1% are reported.

| *Configuration* | $9/2^+$ | $11/2^+$ | $13/2^+$ | $17/2^-$ | $23/2^-$ | $29/2^+$ |
|---|---|---|---|---|---|---|
| $\pi g_{9/2}^{-1}\nu h_{11/2}^{-2}$ | 53.45 | 86.79 | 39.32 | - | - | 100 |
| $\pi g_{9/2}^{-1}\nu d_{3/2}^{-2}$ | 21.08 | 1.20 | 13.65 | - | - | - |
| $\pi g_{9/2}^{-1}\nu s_{1/2}^{-2}$ | 6.24 | - | - | - | - | - |
| $\pi g_{9/2}^{-1}\nu d_{5/2}^{-2}$ | 6.18 | - | 1.33 | - | - | - |
| $\pi g_{9/2}^{-1}\nu g_{7/2}^{-2}$ | 5.31 | - | - | - | - | - |
| $\pi g_{9/2}^{-1}\nu (d_{3/2}^{-1}s_{1/2}^{-1})$ | 1.48 | 3.39 | 19.75 | - | - | - |
| $\pi g_{9/2}^{-1}\nu (g_{7/2}^{-1}d_{3/2}^{-1})$ | - | 1.28 | 3.30 | - | - | - |
| $\pi p_{1/2}^{-1}\nu (d_{3/2}^{-1}h_{11/2}^{-1})$ | - | - | 7.67 | - | - | - |
| $\pi g_{9/2}^{-1}\nu (d_{5/2}^{-1}d_{3/2}^{-1})$ | - | - | 4.27 | - | - | - |
| $\pi g_{9/2}^{-1}\nu (d_{5/2}^{-1}s_{1/2}^{-1})$ | - | - | 3.75 | - | - | - |
| $\pi g_{9/2}^{-1}\nu (d_{3/2}^{-1}h_{11/2}^{-1})$ | - | - | - | 96.28 | 96.47 | - |

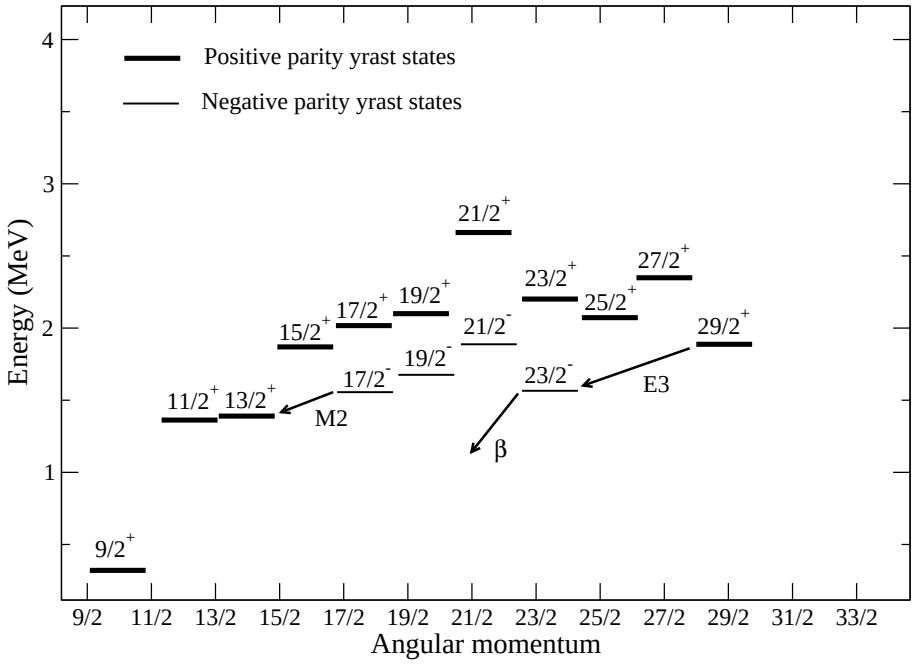


Figure 4.1: Calculated yrast states in $^{129}$In.

note that the first $2^+$ state is overestimated by 162 keV. This is a common feature in this region, and it may be traced to the model-space truncation. The observed decrease in energy of the $29/2^+$ aligned state in $^{129}$In with respect to the $10^+$ in $^{130}$Sn is explained by the strong $p-n$ interaction in the $(\nu h_{11/2}^{-1}\pi g_{9/2}^{-1})_{10^-}$ state. An analogous effect is observed for the other aligned state, $J^\pi = 23/2^-$, of dominant configuration $\pi g_{9/2}^{-1}\nu h_{11/2}^{-1}\nu d_{3/2}^{-1}$. However, this effect is weaker because the $p-n$ interaction in the $(\pi g_{9/2}^{-1}\nu d_{3/2}^{-1})_{6^+}$ state is less attractive than in the $(\pi g_{9/2}^{-1}\nu h_{11/2}^{-1})_{10^-}$ state. The strong decrease in energy of the $23/2^-$ and $29/2^+$ levels is responsible for these two states being long-lived isomers. This is very well reproduced by the shell-model calculation which indeed predicts $\mu$s isomerism for the $17/2^-$ state, $\beta$ isomerism for the $23/2^-$ state and ms isomerism for the $29/2^+$ (see fig. 4.1). The main discrepancy between experiment and theory occurs for the $11/2^+$ level, which is overestimated by 300 keV. This is not surprising since it originates essentially from the coupling of the $2^+$ state in $^{130}$Sn to the $g_{9/2}$ proton hole, the energy of the former, as we have already seen, being overestimated by the theory.

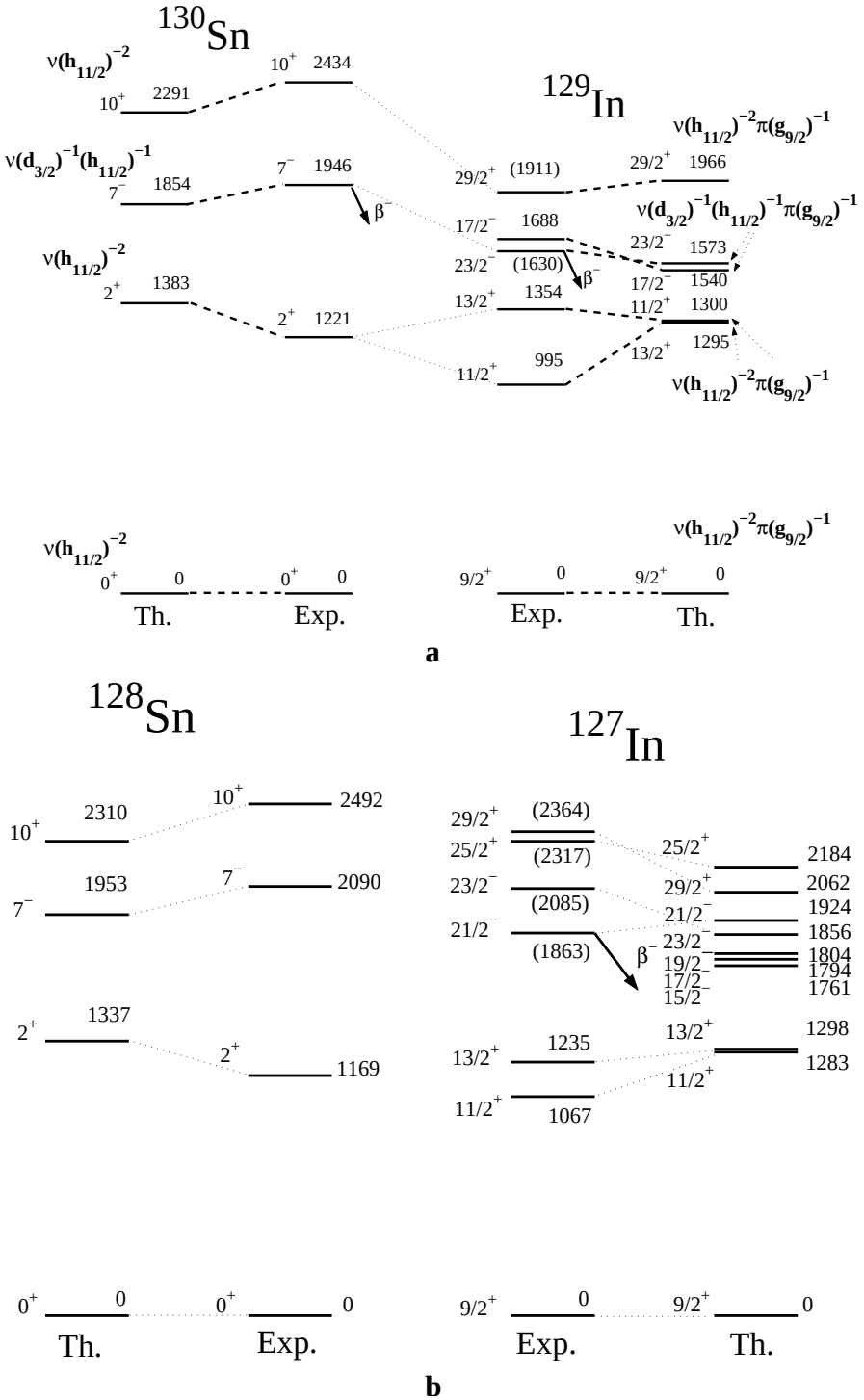


Figure 4.2: Experimental and calculated energies in keV for $^{129}$In and $^{130}$Sn (a) and for $^{127}$In and $^{128}$Sn (b).

### 4.2.2 $^{127}$In

In the case of $^{127}$In two additional neutron holes are present with respect to $^{129}$In. In fig. 4.2b the experimental and calculated levels of $^{127}$In are shown in comparison with $^{128}$Sn. The energies of the yrast states are reported in fig.4.3.

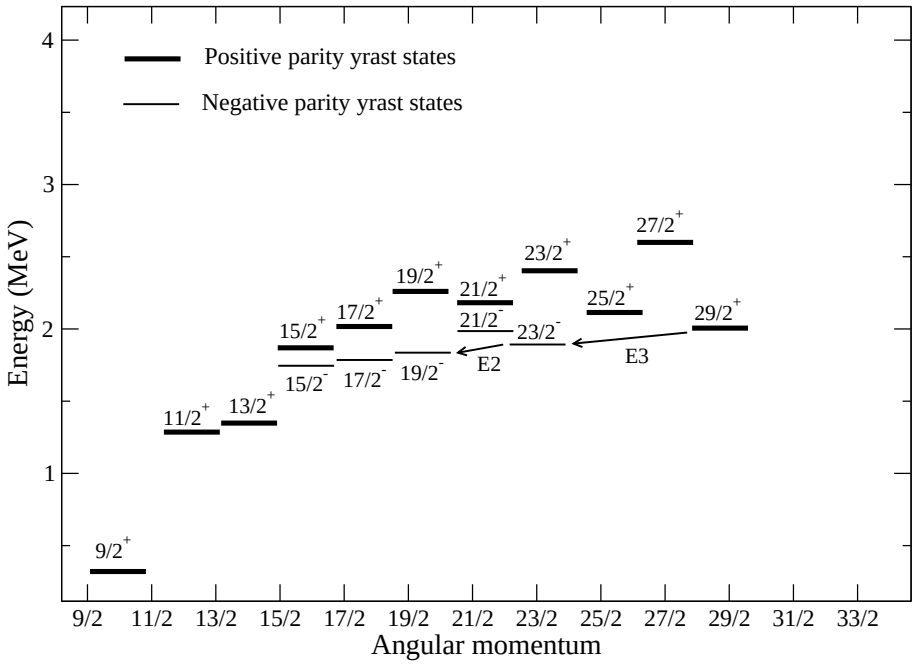


Figure 4.3: Calculated yrast states in $^{127}$In.

It appears that the observed $29/2^+$ and $23/2^-$ states in $^{127}$In are closer to the $10^+$ and $7^-$ in $^{128}$Sn, respectively, as compared to what is shown in fig. 4.2a. This effect could be explained by a decrease in the effects of the $p-n$ interaction from $^{129}$In to $^{127}$In. Another feature possibly related to the effects of the $p-n$ interaction, is the inversion of the $29/2^+$ and $25/2^+$ levels, and the $23/2^-$ and $21/2^-$ levels respectively, in the calculated spectrum of $^{127}$In. As a consequence, a $29/2^+$ ms isomer decaying by an $E3$ transition is predicted, whilst a $\mu$s one decaying by an $E2$ transition is measured, and a $23/2^-$ isomer decaying by an $E2$ transition is predicted, whilst a $21/2^-$ $\beta$-decaying isomer is measured [6]. The theory seems to underestimate the rapid decrease in the effects of the $p-n$ interaction, indicating that the

distribution of the two extra neutron holes may not be properly described. The amplitudes of the main configurations contributing to the calculated levels are reported in table 4.3, where it can be seen that the states of $^{127}$In present a more pronounced configuration mixing with respect to $^{129}$In.

Table 4.3: Amplitudes in % of the main configurations contributing to the wave functions of the $9/2^+$, $11/2^+$, $13/2^+$, $25/2^+$, $29/2^+$ and $15/2^-$, $17/2^-$, $19/2^-$, $21/2^-$ and $23/2^-$ levels of $^{127}$In. Only the amplitudes bigger than 10% are reported.

| *Configuration* | $9/2^+$ | $11/2^+$ | $13/2^+$ | $25/2^+$ | $29/2^+$ |
|---|---|---|---|---|---|
| $\pi g_{9/2}^{-1}\nu h_{11/2}^{-4}$ | 21.3 | 15.3 | 15.6 | 29.1 | 22.7 |
| $\pi g_{9/2}^{-1}\nu d_{3/2}^{-2}\nu h_{11/2}^{-2}$ | 31.2 | 43.5 | 27.3 | 40.6 | 47.9 |
| $\pi g_{9/2}^{-1}\nu s_{1/2}^{-1}\nu d_{3/2}^{-1}\nu h_{11/2}^{-2}$ | - | - | 18.6 | - | - |
| *Configuration* | $15/2^-$ | $17/2^-$ | $19/2^-$ | $21/2^-$ | $23/2^-$ |
| $\pi g_{9/2}^{-1}\nu d_{3/2}^{-2}\nu h_{11/2}^{-3}$ | 63.3 | 58.3 | 26.9 | 67.5 | 54.3 |
| $\pi g_{9/2}^{-1}\nu s_{1/2}^{-2}\nu d_{3/2}^{-1}\nu h_{11/2}^{-1}$ | - | 11.5 | - | - | 12.3 |
| $\pi g_{9/2}^{-1}\nu s_{1/2}^{-1}\nu d_{3/2}^{-2}\nu h_{11/2}^{-1}$ | - | - | - | 17.1 | - |
| $\pi g_{9/2}^{-1}\nu d_{3/2}^{-3}\nu h_{11/2}^{-1}$ | - | - | - | - | 12.7 |

### 4.2.3 Odd-odd In nuclei

Nuclear structure information is very scarce for the heavy odd-odd In nuclei. Nevertheless, the $1^-, 3^+$ and $1^+$ states, resulting from the coupling of a

proton hole $g_{9/2}$ with the neutron holes $h_{11/2}, d_{3/2}$ and $g_{7/2}$, respectively, are experimentally known [2, 50] in $^{126-130}$In. In these three states the neutron and proton are in coplanar orbits and the $p-n$ interaction is expected to be strongly attractive, in particular for the $1^+$ state. A weaker interaction is expected for the $3^+$ state where a $d_{3/2}$ neutron is involved, and this level is used to normalize the level schemes of fig. 4.4.

The shell-model calculations reproduce rather well the relative energies of the three levels in $^{130}$In as well as their evolution when going from $^{130}$In to $^{126}$In. Especially, it is interesting to note the strong variation of the position of the $1^-$ state from $^{130}$In to $^{128}$In. This variation could be explained by a decrease in the effects of $p-n$ interaction when increasing the number of neutron holes. However, as for the aligned $29/2^+$ state in $^{127}$In, the decrease is underestimated by the calculation. The very recent results of a shell-model calculation for $^{130}$In by Dillmann *et al.* [2] are also reported in fig. 4.4 (Th. 2). Although in [2] the two-body matrix elements are derived from the CD-Bonn potential as in this work, the energy of the $1^+$ state is underestimated by 738 keV, which is in strong contrast with the outcome of the calculations presented here. The amplitude of the main configurations contributing to the wave functions of the $3^+$ and $1^-$ levels in $^{130,128}$In are shown in table 4.4. The configuration mixing increases a lot when two neutrons are removed from $^{130}$In.

In conclusion, the shell model reproduces rather well the levels of $^{129}$In and $^{130}$In. However, it underestimates the decrease in the effects of the $p-n$ interaction when two neutrons are removed from $^{130}$In or $^{129}$In. These results show the limits of the predictive power of the present shell-model calculations in the vicinity of $^{132}$Sn for $N < 82$.

### 4.2.4 $M2$ and $E3$ transition probabilities in Sn and In isotopes

In table 4.5, all the available $M2$ and $E3$ transitions in heavy In and Sn isotopes are reported. Among these transitions, only the first one corresponds to a spin change $\Delta$I=3, while all the others have $\Delta$I=2 and $M2/E3$ admixtures are possible.

All these transitions take place between states dominated by configurations which differ by the replacement of an $h_{11/2}$ neutron with a $d_{3/2}$ one, or vice versa. As $M2$ or $E3$ transitions are not possible between these states,

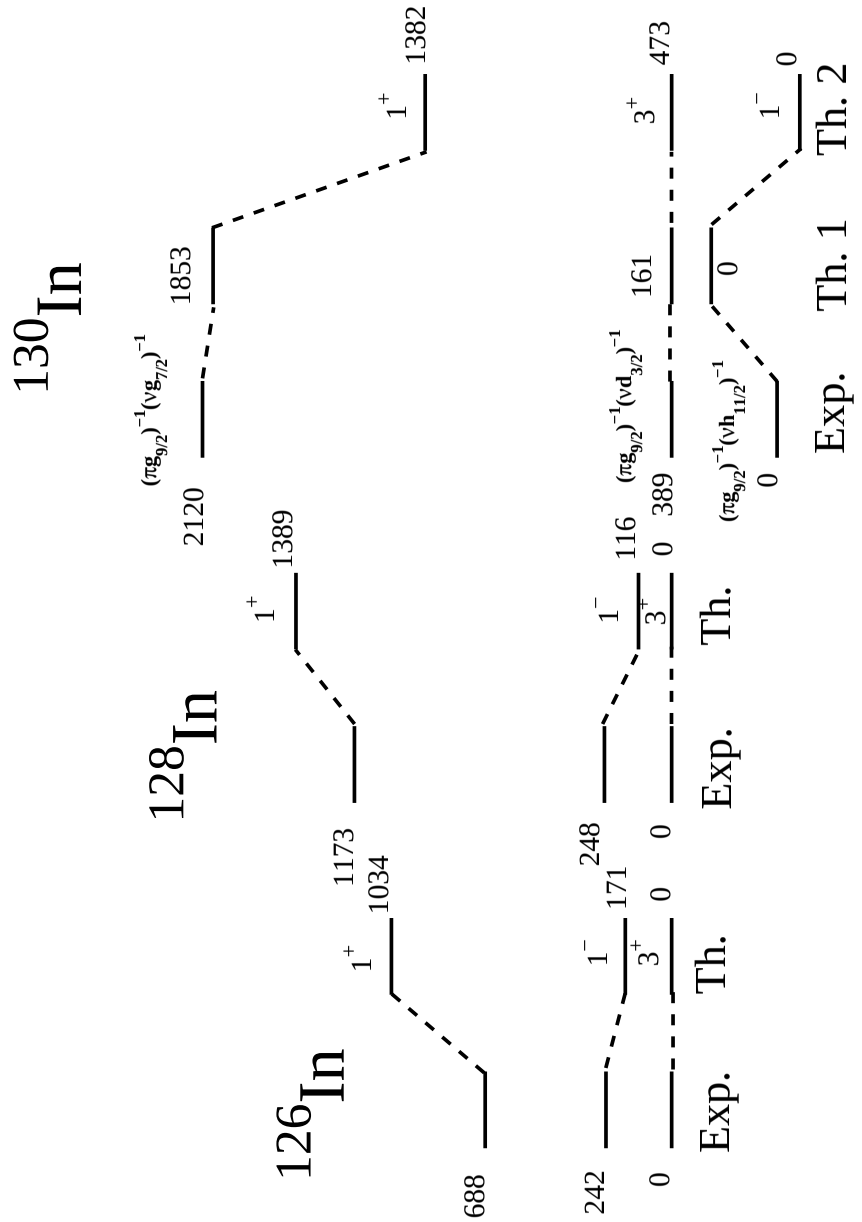


Figure 4.4: Experimental and calculated energies in keV for the odd-odd In.

Table 4.4: Amplitude of the main configurations contributing to the wave functions of the $1^-$ and $3^+$ states in $^{130,128}$In. Only the amplitudes bigger than 2% are reported.

| Nucleus | Configuration | $1^-$ | $3^+$ |
|---|---|---|---|
| $^{130}$In | $\pi g_{9/2}^{-1}\nu h_{11/2}^{-1}$ | 88.13 | - |
| $^{130}$In | $\pi g_{9/2}^{-1}\nu d_{5/2}^{-1}$ | - | 2.99 |
| $^{130}$In | $\pi g_{9/2}^{-1}\nu d_{3/2}^{-1}$ | - | 92.4 |
| $^{130}$In | $\pi f_{5/2}^{-1}\nu h_{11/2}^{-1}$ | - | 3.88 |
| $^{128}$In | $\pi g_{9/2}^{-1}\nu h_{11/2}^{-1}\nu g_{7/2}^{-2}$ | 5.25 | - |
| $^{128}$In | $\pi g_{9/2}^{-1}\nu h_{11/2}^{-3}$ | 31.24 | - |
| $^{128}$In | $\pi g_{9/2}^{-1}\nu d_{5/2}^{-2}\nu h_{11/2}^{-1}$ | 6.54 | - |
| $^{128}$In | $\pi g_{9/2}^{-1}\nu d_{3/2}^{-2}\nu h_{11/2}^{-1}$ | 34.20 | - |
| $^{128}$In | $\pi g_{9/2}^{-1}\nu s_{1/2}^{-2}\nu h_{11/2}^{-1}$ | 7.66 | - |
| $^{128}$In | $\pi g_{9/2}^{-1}\nu d_{5/2}^{-1}\nu h_{11/2}^{-2}$ | - | 2.12 |
| $^{128}$In | $\pi g_{9/2}^{-1}\nu d_{3/2}^{-1}\nu h_{11/2}^{-2}$ | - | 65.70 |
| $^{128}$In | $\pi g_{9/2}^{-1}\nu g_{7/2}^{-2}\nu d_{3/2}^{-1}$ | - | 4.30 |
| $^{128}$In | $\pi g_{9/2}^{-1}\nu s_{1/2}^{-2}\nu d_{3/2}^{-1}$ | - | 4.30 |

admixtures with configurations involving the $g_{7/2}$ or $d_{5/2}$ neutron orbits are necessary. These two orbits are far from the Fermi level in the Sn and In isotopes, and the admixtures are expected to be small. The experimental $B(M2)$ and $B(E3)$ values reported in table 4.5 are obtained assuming pure multipolarities. The very small value $B(E3)$=0.06 W.u. for the $29/2^+ \rightarrow 23/2^-$ transition in $^{129}$In gives the order of magnitude of the $E3$ strength in this region. Consequently, the very large values given in Table III for the other $B(E3)$ transition probabilities in the In isotopes are not realistic, and one may conclude that the transitions have mainly an $M2$ character. By contrast, in the Sn isotopes it is not possible to exclude an $E3$ component in the transitions, and the $M2$ strengths may be smaller than the reported values. It is interesting to note that the $B(M2)$ values are between 10 and 100 times smaller in the Sn isotopes than in the In ones. The results of the shell-model calculations for $^{129}$In predict a $B(M2; 17/2^- \rightarrow 13/2^+) = 0.045$

Table 4.5: Experimental $B(M2)$ and $B(E3)$ values of $M2/E3$ transitions in $^{125,126,128,129,130}$In [32, 33] and $^{123,125,127,129}$Sn [6, 51]. The $B(M2)$ and $B(E3)$ values reported are obtained assuming no admixture of the multipolarities. In the indium isotopes the transitions have predominantly an $M2$ character, whereas in the tin isotopes it is not possible to exclude an $E3$ component, as discussed in the text.

| Nucleus | Energy (keV) | Transition | $B(M2)$ W.u. | $B(E3)$ W.u. |
|---|---|---|---|---|
| $^{129}$In | 281 | $29/2^+ \rightarrow 23/2^-$ | - | 0.06 |
| $^{129}$In | 333.8 | $17/2^- \rightarrow 13/2^+$ | 0.033 | 283 |
| $^{130}$In | 388.8 | $3^+ \rightarrow 1^-$ | 0.047 | 27.6 |
| $^{128}$In | 247.9 | $1^- \rightarrow 3^+$ | 0.047 | 73 |
| $^{126}$In | 243.3 | $1^- \rightarrow 3^+$ | 0.053 | 89 |
| $^{125}$In | 151 | $25/2^+ \rightarrow 21/2^-$ | 0.0015 | 43 |
| $^{129}$Sn | 590 | $19/2^+ \rightarrow 15/2^-$ | $<1.7 \times 10^{-4}$ | 0.49 |
| $^{127}$Sn | 723 | $19/2^+ \rightarrow 15/2^-$ | $1.6 \times 10^{-4}$ | 0.30 |
| $^{125}$Sn | 806 | $19/2^+ \rightarrow 15/2^-$ | $2.9 \times 10^{-4}$ | 0.47 |
| $^{123}$Sn | 838 | $19/2^+ \rightarrow 15/2^-$ | $1.8 \times 10^{-4}$ | 0.29 |

and a $B(E3; 29/2^+ \rightarrow 23/2^-) = 0.052$. These values are in good agreement with the experimental results 0.032(2) W.u. and 0.066(10) W.u., respectively. As regards to the other $B(E3)$ transitions, the calculations predict very small values, typically $10^{-2}$ W.u. for the In isotopes and $10^{-1}$ W. u. for the Sn isotopes.

## 4.3 Cadmium isotopes

### 4.3.1 Even-even Cd isotopes

In the vicinity of the two closed shells of $^{132}$Sn $\mu$s isomers are very abundant and disappear rapidly far from them [1]. In particular, below $Z = 50$ they disappear suddenly for the Cd isotopes, no isomers having been identified up to now in the even-mass nuclei, and only two in the odd-mass nuclei [8, 9]. Neutron-rich $^{126}$Cd and $^{128}$Cd isotopes were recently produced [3] at ISOLDE from the beta-decay of Ag isotopes. However, only the first excited $2^+$ and

$4^+$ states were identified and are shown in fig. 4.5.

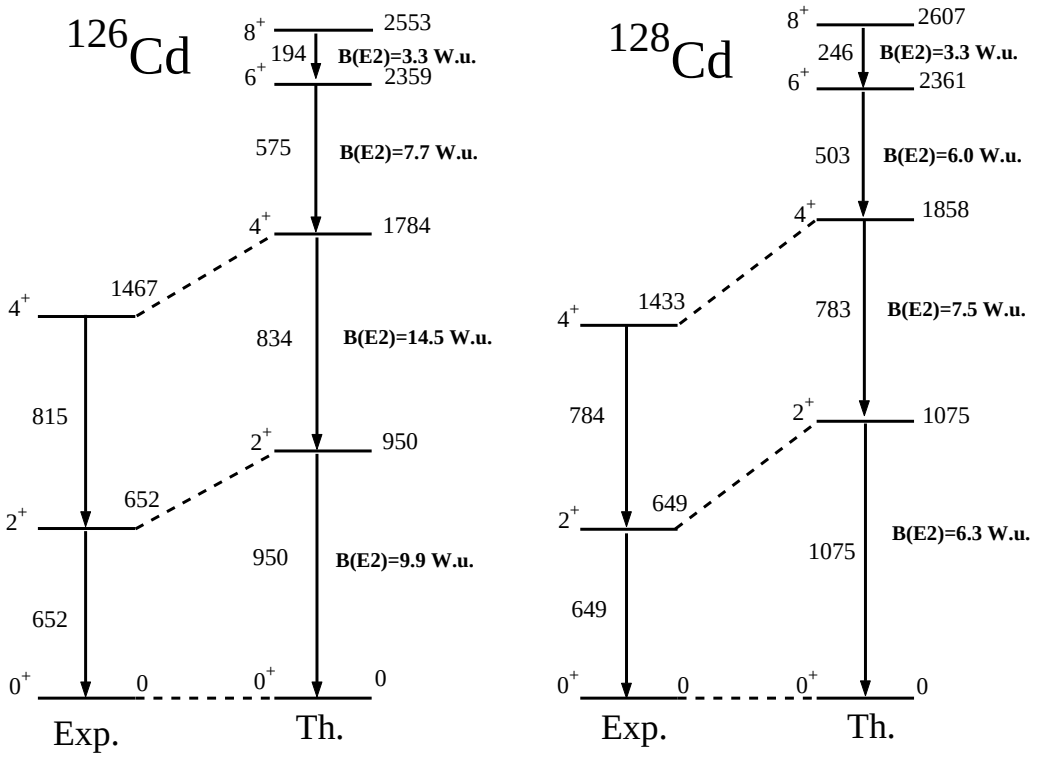


Figure 4.5: Experimental and calculated energies in keV for $^{126,128}$Cd.

The value of $E(4^+)/E(2^+) \sim 2.2$ suggests that some degree of collectivity is present in these two nuclei. The authors of [3] have taken this as a possible evidence for a weakening of the spherical $N$=82 neutron shell below $^{132}$Sn. Our shell-model predictions for these two nuclei are reported in fig. 4.5. The comparison between experiment and theory shows that while the energies of both the $2^+$ and $4^+$ states are overestimated, the $4^+ \rightarrow 2^+$ energy difference is correctly reproduced. The $E2$ transition rates are also reported in fig. 4.5. Unfortunately, it is not possible to compare them with the experimental data, but the $B(E2)$ values and the energy of the $8^+ \rightarrow 6^+$ transitions allow us to predict a half-life of about 10 ns for the $8^+$ state in both Cd isotopes. This value is much shorter than the time of flight of about 2 $\mu$s of the fission fragments through the LOHENGRIN spectrometer and could explain the non-observation of these isomers in our work.

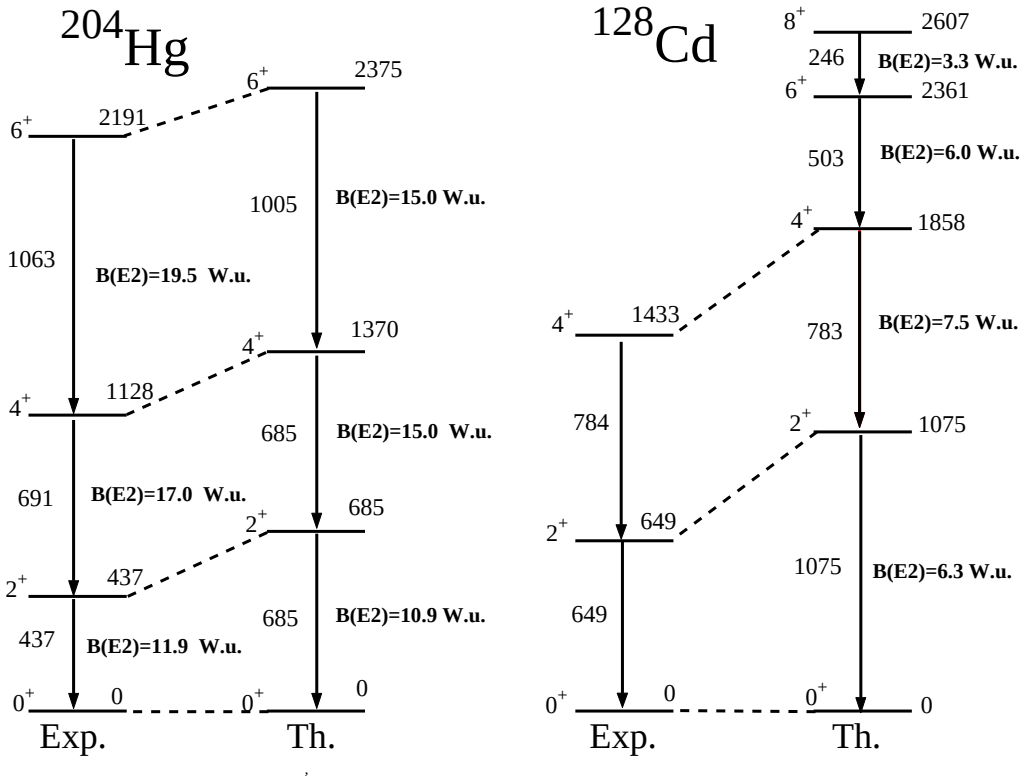


Figure 4.6: Experimental and calculated energies in keV for $^{204}$Hg [52] and $^{128}$Cd.

It is now interesting to compare $^{128}$Cd with $^{204}$Hg (fig. 4.6), since the latter nucleus has two neutron and two proton holes inside doubly-magic $^{208}$Pb (fig. 4.6) and possesses some degree of collectivity. For $^{204}$Hg, which is easier to study because it is on the line of stability, the energy levels and $E2$ transition rates have been reported in the literature [52]. This nucleus presents a nice collective band based on the ground state and is characterized by a $E(4^+)/E(2^+) \sim 2.6$ ratio, which is larger than the one measured in $^{128}$Cd. Rydström *et al.* [52] have shown that for $^{204}$Hg the energy levels and the $E2$ transition rates up to the $6^+$ state are well reproduced by the shell model. These authors have also predicted that the collective band ends at the $8^+$ state and that the states up to the $6^+$ are mostly built from the low-spin single-hole $s_{1/2}$ and $d_{3/2}$ orbits for the protons, and $p_{1/2}$, $f_{5/2}$ and

$p_{3/2}$ orbits for the neutrons. Both these sets of single-parity states are close to the Fermi level, and this can explain the collectivity. The unique parity states have about 1.5 MeV of excitation energy and don't participate to the observed excitations. The situation is different in $^{128}$Cd, because the unique-parity states $h_{11/2}$ and $g_{9/2}$ are very close to the Fermi level. This feature plays an important role in the structure of this nucleus, and could perhaps explain its weaker collectivity. The present information are however too scarce to conclude that the collectivity is a consequence of the shell structure and more experimental data are needed to clarify the situation.

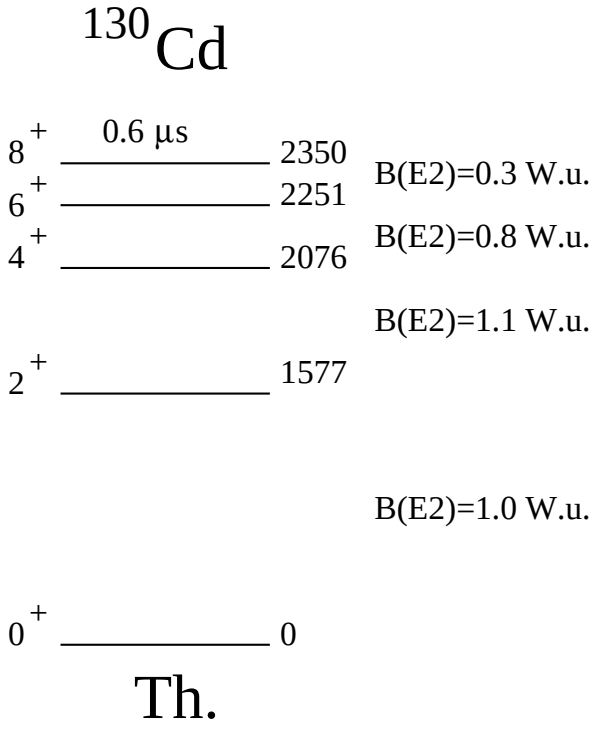


Figure 4.7: Calculated levels, transition probabilities and lifetime of $^{130}$Cd. The energies are in keV.

In $^{130}$Cd no excited levels are experimentally known up to now. In fig. 4.7 the results of the shell-model calculation are reported. The small energy difference between the $8^+$ and $6^+$ states would cause the first one to be a $\mu$s isomer. The predicted half-life of 0.6 $\mu$s, very close to the LOHENGRIN

Table 4.6: Amplitudes in % of the main configurations contributing to the wave functions of the $0^+$, $2^+$, $4^+$, $6^+$ and $8^+$ and levels of $^{130,128}$Cd. Only the amplitudes bigger than 6% are reported.

| Nucleus | Configuration | $0^+$ | $2^+$ | $4^+$ | $6^+$ | $8^+$ |
|---|---|---|---|---|---|---|
| $^{130}$Cd | $\pi g_{9/2}^{-2}$ | 78.5 | 95.2 | 99.4 | 100.0 | 100.0 |
| $^{130}$Cd | $\pi p_{3/2}^{-2}$ | 7.0 | - | - | - | - |
| $^{130}$Cd | $\pi p_{1/2}^{-2}$ | 8.7 | - | - | - | - |
| $^{128}$Cd | $\pi g_{9/2}^{-2}\nu h_{11/2}^{-2}$ | 37.2 | 44.5 | 37.2 | 62.1 | 59.8 |
| $^{128}$Cd | $\pi g_{9/2}^{-2}\nu d_{3/2}^{-2}$ | 15.6 | 10.1 | 6.8 | 7.1 | 9.8 |

detection limit of $\sim 0.5$ $\mu$s, along with the already mentioned low yield (see section 3.5), makes a measurement of this nucleus very difficult using the LOHENGRIN spectrometer. The calculated levels of $^{130}$Cd are predicted to be almost pure members of the multiplet $\pi g_{9/2}^{-2}$, as the weight of this configuration is larger than 80% for all the states. The situation of $^{128}$Cd is different, indeed a significant configuration mixing is present in all the levels. The weight of the dominant configurations ($\pi g_{9/2}^{-2}$ coupled with $\nu h_{11/2}^{-2}$ or $\nu d_{3/2}^{-2}$) is never larger than 60%. The amplitudes of the main configurations contributing to the wave functions of $^{130,128}$Cd are reported in table 4.6.

### 4.3.2 $^{125}$Cd

In chapter 3 a tentative level scheme of $^{125}$Cd has been proposed by analogy with its neighbor $^{123}$Cd and a shell model calculation on $^{127}$Cd (see fig. 4.8). Unfortunately the number of configurations in $^{125}$Cd is too high to perform a calculation using the OXBASH code, therefore only $^{127}$Cd was computed. For this nucleus the theory predicts the $19/2^+$ state to be a $\mu$s isomer, decaying by an $M2$ transition to the $15/2^-$ state, which decays itself to the $11/2^-$ $\beta$ isomer. The origin of $\mu$s isomerism is the inversion between the $19/2^+$ and the $19/2^-$ levels going from $^{123}$Cd to $^{127}$Cd. If the structure of $^{125}$Cd is similar to the structure of $^{127}$Cd, the presence of the isomeric cascade in $^{125}$Cd is explained. The deduced transition probabilities in case of pure multipolarities ($B(M2) = 4.5 \times 10^{-5}$ W.u., $B(E3) = 0.7$ W.u.) suggest a

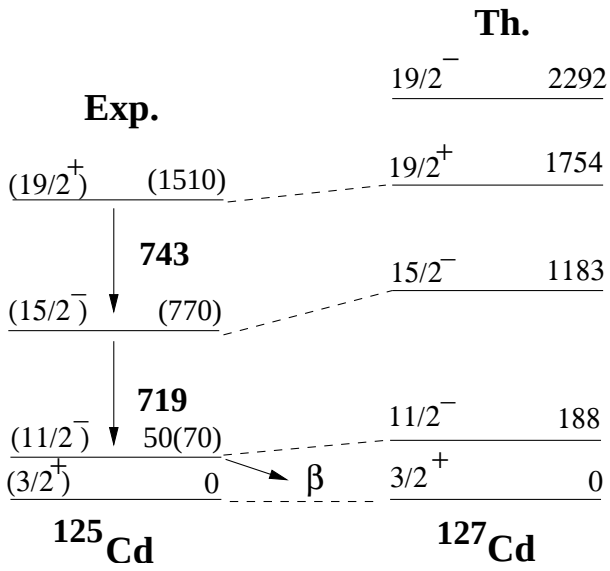


Figure 4.8: Experimental levels of $^{125}$Cd in comparison with a theoretical calculation of $^{127}$Cd. The energies are in keV.

possible $M2/E3$ mixing for the isomeric transition.

# Conclusions

Up to now, for several of the nuclei investigated only some excited states were known, but no substantial spectroscopic information such as level-schemes, transition probabilities, lifetimes etc... were available. The present work has enriched the very scarce experimental knowledge on indium and cadmium isotopes in the mass range $A$=123 to 130, by means of delayed $\gamma$-rays and conversion-electron measurements of fission products. Consequently, level schemes have been proposed for $^{123,125,127,129}$In and $^{125}$Cd. Moreover, new half-lives were measured for $^{123,129}$In and several half-lives known with large uncertainties were remeasured for $^{126,127,128,129,130}$In and $^{125}$Cd. An upper limit of 0.5 $\mu$s, for the half-life of the $8^+$ state in $^{126,128}$Cd has been given. The transition probability assuming pure $M2$ multipolarity was measured in $^{126,128,130}$In and $^{125}$Cd. It was shown that the $M2$ transitions are much faster in the In isotopes than in the proton-magic Sn isotopes. Also $^{125}$Cd seems to present a behavior similar that one of Sn nuclei, indeed the $M2$ strength appears to be reduced with respect to the In nuclei. A possible $M2/E3$ admixture is foreseen for the Sn and Cd mentioned, but it seems to be unlikely for the odd-odd In isotopes studied and $^{129}$In.

Along with the experimental work, shell-model calculations, using a realistic interaction derived from the Cd-Bonn $NN$ potential, were performed for the odd-even nuclei $^{127,129}$In and $^{127,129}$Cd, for the odd-odd nuclei $^{126,128,130}$In, and for the even-even nuclei $^{126,128,130}$Cd. These calculations provide a satisfactory interpretation of $^{129,130}$In, but some discrepancies occur for the lighter In isotopes. By comparing experiment and theory, the dominant configurations of all the states observed have been found. They appear to be dominated by the unique parity states $\pi g_{9/2}$ and $\nu h_{11/2}$ very close to the Fermi level, coupled with the $\nu d_{3/2}$ orbitals, whose energy is also close to the Fermi level. It is interesting to follow the evolution of the energy of the aligned configurations $(\pi g_{9/2}^{-1}\nu h_{11/2}^{-2})_{29/2^+}$, $(\pi g_{9/2}^{-1}\nu h_{11/2}^{-1}\nu d_{3/2}^{-1})_{23/2^-}$ and $(\pi g_{9/2}^{-1}\nu h_{11/2}^{-1}\nu d_{3/2}^{-1})_{17/2^-}$

in $^{127,125,123}$In, where two, four or six neutrons are removed from $^{129}$In. The observed $17/2^-$ state in $^{129}$In is isomeric, due to the strong $p-n$ interaction in the aligned $(\pi g_{9/2}\nu h_{11/2})_{10^-}$ configuration, coupled with an additional neutron hole in the $\nu h_{11/2}$ orbital. Such a strong interaction makes the $17/2^-$ level a low-lying level, therefore it can only decay by an hindered $M2$ transition to the $13/2^+$ state, as can be clearly seen in fig. 4.1. In $^{123,125}$In the strength of the $p-n$ interaction decreases, resulting in an increase of the energy of the $17/2^-$ state relatively to the other low-lying levels. Consequently, there are other states lower in energy in the level scheme, indeed the observed $17/2^-$ decays via an $E2$ isomeric transition to the $13/2^-$ state in $^{123}$In, and via an $M1$ transition to the $15/2^-$ state in $^{125}$In. In $^{127}$In the $17/2^-$ was not experimentally observed. The theory predicts a situation analogous to $^{125}$In, where the energy difference between $17/2^-$ and the $15/2^-$ state is very small ($< 50$ keV). The $29/2^+$ and $23/2^-$ states were observed and calculated only in $^{127,129}$In. They result from the coupling of a proton hole in $g_{9/2}$ with the two neutron hole states $10^+$ and $7^-$ in $^{128}$Sn and $^{130}$Sn respectively. The comparison between $^{128}$Sn - $^{127}$In and $^{130}$Sn - $^{129}$In (see fig. 4.2) shows a pronounced decrease of the $p-n$ interaction strength going from $^{129}$In to $^{127}$In. Indeed the $29/2^+$ and $23/2^-$ states are more close to the $10^+$ and $7^-$ states in the former nucleus with respect to the latter one. The theory seems to underestimate this effect, with dramatic consequences on the predicted structure of $^{127}$In, no longer reproduced. A similar effect is observed in the even-mass $^{126,128,130}$In. The aligned levels have spin and parity $1^-$, $3^+$ and $1^+$ resulting from the $\pi g_{9/2}^{-1}\nu h_{11/2}^{-1}$, $\pi g_{9/2}^{-1}\nu d_{3/2}^{-1}$, and $\pi g_{9/2}^{-1}\nu g_{7/2}^{-1}$ configurations respectively, coupled to zero, two and four additional neutron holes. The inversion of the $1^-$ and $3^+$ states in $^{126,128}$In with respect to $^{130}$In is reproduced by the theory, but the calculated energy difference is smaller than the experimental findings. This could be again due to an underestimation of the rapid decrease of the $p-n$ interaction strength when two or more neutrons are removed from $^{129,130}$In.

The calculations for $^{126,128}$Cd predict short half-lives ($\sim 10$ ns) for the $8^+$ states, which could explain why they have not been observed in the present work. It was shown that these nuclei present some similarities to $^{204}$Hg. The two nuclei $^{128}$Cd and $^{204}$Hg have only two proton and two neutron holes inside doubly-magic cores, $^{132}$Sn and $^{208}$Pb respectively, and have collective behavior. In the second nucleus, this effect can be explained by the presence of several single-particle orbitals close to the Fermi level, but it is not the case of Cd isotopes. The hypothesis of shell quenching was proposed by Dillmann

*et al.* in [2], who first observed the excited states in $^{126,128}$Cd. The shell model calculation performed in this work predict some degree of collectivity for these two nuclei, but it overestimates the energy of the first $2^+$ states, while it reproduces the energy difference between the $4^+$ and the $2^+$ states correctly. Whether this effect is a consequence of the weakening of the shell closure or not is not yet clear. More experimental data, in particular $B(E2)$ transition probabilities, are necessary to clarify the situation. Evidence of collectivity in $^{130}$Cd would give a clear sign of shell quenching in the region, but unfortunately this nucleus is very difficult to produce and study at the ILL. Very recently (September 2004) an experiment has been performed in CERN, Geneva, using the MINIBALL array to measure $B(E2)$ transition probabilities in $^{122,124,126}$Cd by means of Coulomb excitation. The work is still in progress, therefore the results cannot be quoted in this thesis, but hopefully they will help to shed light on the strength of the shell closure in neutron rich nuclei close to $^{132}$Sn. To further investigate the odd-even Cd isotopes an experiment is planned for the beginning of 2005 at the ILL reactor in Grenoble, where the experimental part of this work has been carried out. The efficiency for $\gamma$-ray detection will be improved using two Clover detectors.

# Bibliography


[1] J. A. Pinston and J. Genevey, J. Phys. G **30**, R57 (2004).

[2] I. Dillmann, K. L. Kratz, A. Wøhr, O. Arndt, B. A. Brown, P. Hoff, M. Hjorth-Jensen, U. Köster, A. N. Ostrowski, B. Pfeiffer, et al., Phys. Rev. Lett. **91**, 162503 (2003).

[3] T. Kautzsch, W. B. Walters, M. Hannawald, K.-L. Kratz, V. I. Mishin, V. N. Fedoseyev, W. Böhmer, Y. Jading, P. Van Duppen, B. Pfeiffer, et al., Eur. Phys. J. A **9**, 201 (2000).

[4] H. Huck, A. Jech, G. Martí, M. L. Pérez, J. J. Rossi, and H. M. Sofía, Phys Rev. C **39**, 997 (1989).

[5] P. Hoff, B. Ekström, and B. Fogelberg, Nucl. Phys. **A 459**, 35 (1986).

[6] H. Gausemel, B. Fogelberg, T. Engeland, M. Hjorth-Jensen, P. Hoff, H. Mach, K. A. Mezilev, and J. P. Omtvedt, Phys. Rev. C **69**, 054307 (2004).

[7] B. Fogelberg, H. Mach, H. Gausemel, J. P.Omtved, and K. A. Mezilev, in *Nuclear Fission and Fission-Product Spectroscopy*, edited by G. Fioni, H. Faust, S. Obersted, and F. Hambsch (American Institute of Physics, 1998), AIP Conference Proceedings 447, p. 191.

[8] M. Hellström, M. N. Mineva, A. Blazhev, H. J. Boardman, J. Ekman, K. Gladnishki, H. Grawe, J. Gerl, R. Page, Z. Podolyak, et al., in *Proc. Third Int. Conf. Fission and Properties of the Neutron-Rich Nuclei*, edited by J. Hamilton, A. Ramayya, and H. Carter (World Scientific, 2003), p. 22.

[9] M. Hellström, M. N. Mineva, A. Blazhev, H. J. Boardman, J. Ekman, J. Gerl, K. Glandishki, H. Grawe, R. Page, Z. Podolyak, et al., in *Nuclear structure and dynamics at the limits: proceedings of the International Workshop XXXI on Gross Properties of Nuclei and Nuclear Excitations: Hirschegg, Austria, January 12-18, 2003*, edited by H. Feldmeier (Imprint Darmstadt : Gesellschaft für Schwerionenforsching (GSI), 2003), p. 72.

[10] R. Machleidt, Phys. Rev. C **63**, 024001 (2001).

[11] A. Gargano, Eur. Phys. J. A **20**, 103 (2004).

[12] L. Coraggio, A. Covello, A. Gargano, N. Itaco, and T. T. S. Kuo, Phys. Rev. C **66**, 064311 (2002).

[13] E. Moll, H. Schrader, G. Siegert, H. Hammers, M. Asghar, J. P. Bocquet, P. Armbruster, H. Ewald, and H. Wollnik, Kerntechnik **19**, 374 (1977).

[14] O. Hahn, Berichte der Deutschen Chemischen Gesellschaft **54**, 1131 (1921).

[15] C. von Weizsäcker, Naturwiss. **24**, 813 (1936).

[16] A. Bohr and B. R. Mottelson, *Nuclear Structure* (W. A. Benjamin, Inc., 1969).

[17] P. Walker and G. Dracoulis, Nature **35**, 399 (1999).

[18] P.Chowdhury, B.Fabricius, C.Christensen, F.Azgui, S.Bjornholm, J.Borggreen, A.Holm, J.Pedersen, G.Sletten, M.A.Bentley, et al., Nucl. Phys. **A485**, 136 (1988).

[19] H. C. Pauli, K. Alder, and R. M. Steffen, in *The electromagnetic interaction in nuclear spectroscopy*, edited by W. D. Hamilton (North-holland publishing company, 1975), p. 341.

[20] M. Göppert Mayer, Phys. Rev. **75**, 1969 (1949).

[21] O. Haxel, J. H. D. Jensen, and H. E. Suess, Phys. Rev. **75**, 1766 (1949).

[22] M. Göppert Mayer and J. H. D. Jensen, *Elementary Theory of Nuclear Shell Structure* (Wiley, New York, 1995).

[23] J. W. Grüter, K. Sistemich, P. Armbruster, J. Eidens, and H. Lawin, Phys. Lett. B **33**, 474 (1970).

[24] I. Tsekhanovich, N. Varapai, V. Rubchenya, G. S. Simpson, V. Solokov, G. Fioni, and Ilham Al Mahamid, Phys. Rev. C **70**, 1 (2004).

[25] U. Brosa, S. Grossmann, and A. Müller, Phys. Rep. **197**, 167 (1990).

[26] I. D. Alkhazov, B. F. Gerasimenko, and A. V. Shpakov, Yad. Fiz. **48**, 1635 (1988).

[27] V. A. Rubchenya and J. Äystö, *Eurisol research project*, http://ganil.fr/eurisol.

[28] H. Faust, Eur. Phys. J. A **14**, 459 (2002).

[29] H. Faust and Z. Bao, Nucl. Phys. **A736**, 55 (2004).

[30] A. Iljinov, M. Mebel, N. Bianchi, E. De Sanctis, C.Guaraldo, V. Lucherini, V. Muccifora, E.Polli, A. Reolon, and P.Rossi, Nucl.Phys. **A543**, 517 (1992).

[31] A. Gavron, in *Computational Nuclear Physics*, edited by K. Langanke, J. Maruhn, and S. Koonin (Springer-Verlag, New York, 1993), vol. 2, p. 108.

[32] A. Scherillo, J. Genevey, J. A. Pinston, A. Covello, H. Faust, A. GArgano, R. Orlandi, G. S. Simpson, I. Tsekhanovich, and N. Warr, Phys. Rev. C **70**, 054318 (2004).

[33] J. Genevey, J. A. Pinston, H. R. Faust, R. Orlandi, A. Scherillo, G. S. Simpson, I. S. Tsekhanovich, A. Covello, A. Gargano, and W. Urban, Phys. Rev. C **67**, 054312 (2003).

[34] J. Ziegler, J. Biersack, and U. L. Press, *The Stopping and Range of Ions and Solids* (Pergamon Press, New York, 1996).

[35] G. Duchêne, F. A. Becka, P. J. Twinb, G. de France, D. Curiena, L. Hana, C. W. Beausang, M. A. Bentley, P. J. Nolan, and J. Simpson, Nucl. Instr. & Meth. A **432**, 90 (1999).

[36] P. Reiter, J. Ebert, H. Faust, S. Franchoo, J. Gerld, C. Gund, D. Habs, M. Huyse, A. Jungclaus, K. P. Lieb, et al., Nucl. Phys. A **701**, 209 (2002).

[37] R. H. Mayer, D. T. Nisius, I. G. Bearden, P. Bhattacharyya, L. Ritchter, M. Sferrazza, Z. W. Grabowski, P. J. Daly, B. Fornal, I. Ahmad, et al., Phys. Lett. B **336**, 308 (1994).

[38] J. A. Pinston, C. Foin, , J. Genevey, R. Béraud, E. Chabanat, H. Faust, S. Oberstedt, and B. Weiss, Phys. Rev. C **61**, 024312 (2000).

[39] B.Fogelberg, in *Proc. Intern. Conf. Nuclear Data for Science and Technology, Mito, Japan* (1988), p. 837.

[40] H. Mach, R. L. Gill, D. D. Warner, , and A. Piotrowski, Phys. Rev. C **34**, 1117 (1986).

[41] B. A. Brown, A. Etchegoyen, and W. D. M. Rae, MSU-NSCL (Report No. 524).

[42] T. Kuo and G. E. Brown, Nucl. Phys. **85**, 40 (1966).

[43] G. H. Herling and T. T. S. Kuo, Nucl. Phys. **A181**, 113 (1972).

[44] T. Hamada and I. D. Johnston, Nucl. Phys. **34**, 382 (1962).

[45] J. B. McGory and T. T. S. Kuo, Nucl. Phys. **A247**, 283 (1975).

[46] V. G. J. Stoks, R. A. M. Klomp, M. C. M. Rentmeester, and J. J. de Swart, Phys. Rev. C **48**, 792 (1993).

[47] R. Machleidt, *The high-precision, charge-dependent, bonn nucleon-nucleon potential (cd-bonn)*, arXiv:nucl-th/0006014.

[48] M. Hannawald, K.-L. Kratz, B. Pfeiffer, W. B. Walters, V. N. Fedoseyev, V. I. Mishin, W. F. Mueller, H. Schatz, J. V. Roosbroeck, U. Köster, et al., Phys. Rev. C **62**, 054301 (2000).

[49] L. Coraggio, A. Covello, A. Gargano, N. Itaco, and T. T. S. Kuo, J. Phys. G **26**, 1697 (2000).

[50] L. Spanier, K. Aleklett, B. Ekstrom, and B. Fogelberg, Nucl. Phys. **A474**, 359 (1987).

[51] J. A. Pinston, C. Foin, J. Genevey, R. Béraud, E. Chabanat, H. Faust, S. Oberstedt, and B. Weiss, Phys. Rev. C **61**, 024312 (2000).

[52] L. Rydstrom, J. Blomqvist, R. J. Liotta, and C. Pomar, Nucl. Phys. **A512**, 217 (1990).

# Acknowledgements

It is a pleasure for me to thank all the people to whom I am indebted for their help. Many thanks to:

Prof. Dr. Jan Jolie for his supervision, and for giving me the possibility to participate to several experiments at large scale facilities, such as MINIBALL@CERN.

Dr. Jean Alain Pinston for teaching me all what I know about isomers, the fruitful discussions, and his precious help during the whole thesis work.

Dr. Janine Genevey, without her I would have never known how to get lifetimes, nice spectra etc... from raw data.

Prof. Dr. Hans Börner, the "bridge" between me and the Cologne University, for having accepted me in the nuclear Physics group at ILL, Grenoble.

Dr. Herbert Faust and Dr. Gary Simpson for supervising me at ILL.

Dr. Gary Simpson, Dr. Igor Tsekhanovich, Dr. Herbert Faust, Dr. Paolo Mutti and Drd. Riccardo Orlandi for the stimulating discussions about Physics, politics and society during the lunch and tea time at ILL.

Prof. Aldo Covello and Dr. Angela Gargano for introducing me in the world of the shell-model calculations.

Dr. Jurghen Eberth, Dr. Dirk Weißhaar and Dr. Heinz-Georg Thomas for making me discover a very important aspect of nuclear Physics: the complexity of germanium detectors.

Dr. Igor Tsekhanovich, Rene Guglielmini, Norbert Laurens, and all the technicians of ILL for making the experiments possible.

Dr. Karl-Oskar Zell, without him the german burocracy would have killed me.

Dr. Jean Alain Pinston, Dr. Gary Simpson and Drd. Bart Bruyneel for the careful reading of the manuscript, valuable comments and corrections.

Dr. George Pascovici for his help in any problem related with electronic I faced and his warm moral support.

All the colleagues and friends of ILL and IKP for the nice atmosphere and the beautiful time spent together.

Barbara Melon, Irina Stefanescu, Riccardo Orlandi, Roberta Cuozzo, for standing by me and showing me the best aspect of friendship.

My grandfather, my mother, my brother, my cousin Isabella and all my family for their love and patience.

And, -most of all-, Alessandro Bombardi, for having encouraged me to start this work, his love and constant support.

# Erklärung

Ich versichere, dass ich die von mir vorgelegte Dissertation selbständing angefertigt, die benutzten Quellen und Hilfsmittel vollständig angegeben und die Stellen der Arbeit - einschließlich Tabellen, Karten und Abbildungen -, die anderen Werken im Wortlaut oder dem Sinn nach entnommen sind, in jedem Einzelfall als Entlehnung kenntlich gemacht habe; dass diese Dissertation noch keiner anderen Fakultät oder Universität zur Prüfung vorgelegen hat; dass sie - abgesehen von unten angegebenen Teilpublikationen - noch nicht veröffentlicht worden ist sowie, dass ich eine solche Veröffentlichung vor Abschluss des Promotionsverfahrens nicht vornehmen werde. Die Bestimmungen dieser Promotionsordnung sind mir bekannt. Die von mir vorgelegte Dissertation ist von Prof. Dr. Jan Jolie betreut worden.

Teilveröffentlichungen:

- "Neutron Rich In and Cd close to the magic $^{132}$Sn", A. Scherillo, G. Genevey, J.A. Pinston, A. Covello, H. Faust, A. Gargano, R. Orlandi, G. S. Simpson, I Tsekhanovich, N. Warr, Phys. Rev. C **70**, 054318 (2004)
- "High-spin microsecond isomers in $^{129}$In and $^{129}$Sb", G. Genevey, J. A. Pinston, H. Faust, R. Orlandi, A. Scherillo, G.S. Simpson, I. Tsekhanovich, A. Covello, A. Gargano and W. Urban, Phys. Rev. C **69**, 054312 (2003)

# Lebenslauf

| | |
|---|---|
| **Name** | Antonella Scherillo |
| **Geburtsdatum/-ort** | 10.08.1972 in Neapel, Italien |
| **Nationalität** | italienisch |
| **Familienstand** | ledig |

**Schulbildung:**

| | |
|---|---|
| 77–82 | Scuola elementare, Neapel, Italien |
| 82–85 | Scuola media statale "Vincenzo Irolli", Neapel, Italien |
| 85–90 | Liceo scientifico "Leon Battista Alberti", Neapel, Italien |
| 20/07/90 | Abitur |

**Hochschulstudium:**

| | |
|---|---|
| 09/90 | Immatrikulation an der Universität zu Neapel für das Studienfach Physik |
| 13/12/00 | Diplom im Fach Physik mit dem Thema: "Studio della dinamica della fissione nel sistema $^{32}S + {}^{100}Mo$ a $E_{lab} = 240\,MeV$" |
| 06/01 | Beginn der Promotion, Fach Physik an der Universität zu Köln |

**Arbeitsverhältnisse:**

| | |
|---|---|
| Seit 06/01 | Wissenschaftliche Mitarbeiterin am Institut für Kernphysik der Universität zu Köln |
| 12/01–12/04 | 1/2 Doktorandenstelle des ILL-Grenoble |